

# Capturing Individual Hydrogen Bond Strengths in Ices via Periodic Local Vibrational Mode Theory: Beyond the Lattice Energy Picture

Sadisha Nanayakkara,<sup>†</sup> Yunwen Tao,<sup>†</sup> and Elfi Kraka<sup>\*</sup>



Cite This: *J. Chem. Theory Comput.* 2022, 18, 562–579



Read Online

ACCESS |



Metrics & More



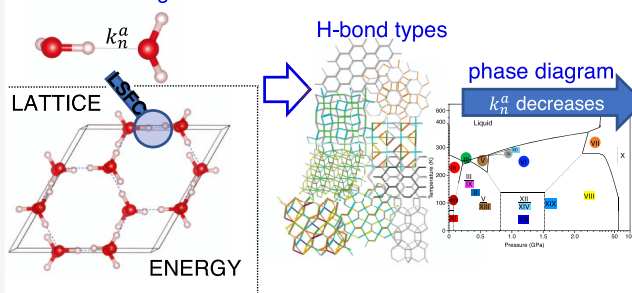
Article Recommendations



Supporting Information

**ABSTRACT:** Local stretching force constants derived from periodic local vibrational modes at the vdW-DF2 density functional level have been employed to quantify the intrinsic hydrogen bond strength of 16 ice polymorphs, ices *Ih*, II, III, IV, V, VI, VII, VIII, IX, XI, XII, XIII, XIV, XV, XVII, and XIX, that are stable under ambient to elevated pressures. Based on this characterization on 1820 hydrogen bonds, relationships between local stretching force constants and structural parameters such as hydrogen bond length and angle were identified. Moreover, different bond strength distributions, from uniform to inhomogeneous, were observed for the 16 ices and could be explained in relation to different local structural elements within ices, that is, rings, that consist of different hydrogen bond types. In addition, criteria for the classification of hydrogen bonds as strong, intermediate, and weak were introduced. The latter was used to explore a different dimension of the water–ice phase diagram. These findings will provide important guidelines for assessing the credibility of new ice structures.

## Local Stretching Force Constant



## 1. INTRODUCTION

Ice, the condensed state of water, is a solid presence on the Earth's surface and its interiors and, moreover, can be found across the entire solar system<sup>1–4</sup> and beyond; within comets, moons, distant planets, rings of giant planets, and even in interstellar medium.<sup>5–7</sup> The most frequently observed form of ice, or ice polymorph, at ambient pressure on earth is hexagonal ice, *Ih*.

Hydrogen bonding is pivotal to determine the structure of H<sub>2</sub>O ices and the prospect of each water molecule participating in four hydrogen bonds, (H-bond)s, has led to the rich variety of ice polymorphs.<sup>8–13</sup> The local tetrahedral coordination around each water molecule, also called the Walrafen pentamer,<sup>14</sup> results in six possible orientations that can be adopted by the central and neighboring water molecules. The sole constraints that govern the arrangement of water molecules are the Bernal–Fowler ice rules,<sup>15</sup> and consequently, a large number of allowed configurations exist for one ice phase near its true ground state. This is known as hydrogen disorder, where the oxygen sublattice preserves an order while the respective H-positions around the oxygen atoms are occupied arbitrarily, that is, H-sites have equal occupancy of 0.5. Upon cooling, the H-disordered ices undergo a phase transition into their H-ordered counterparts, giving rise to a hydrogen order–disorder ice pair because both correspond to the same H-bond network topology.

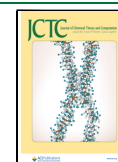
Experimental and theoretical studies that cover the manifold aspects and implications of H-bond network in ices are prolific, ranging from spectroscopical analyses<sup>16–20</sup> to thermodynamics of proton ordering.<sup>21–23</sup> These studies are concentrated on the

actual cooperative arrangement of the water molecules<sup>24–26</sup> and its influence on macroscopic properties of ice such as structure, density, electrical, thermal, and lattice dynamics, rather than on hydrogen bonding, an important microscopic aspect.

Noteworthy in this connection is the use of electron localization function (ELF) scheme by Silvi and Ratajczak<sup>27</sup> to characterize the H-bond strength of H-bonded crystals, including ice VIII. Based on ELF profiles along the O–H...O bond line, the presence of a weak H-bond was suggested in the case of ice VIII, which was determined to be weaker than that of a water dimer and a pentamer. Moreover, on the grounds of a linear relationship between ELF values at the H-bond interaction point and pressure, they proposed ice X, which occurs over 60 GPa to be constituted of very strong H-bonds. In this context, Murray and Galli<sup>28</sup> examined the difference of the electron densities  $\Delta(\rho)$  for cubic ice Ic and ice VIII to gain insights into hydrogen bond strength variation as a function of pressure and arrived at similar conclusions that hydrogen bond weakening takes place in high-pressure ices such as ice VIII. Another important study that provides a different perspective of the H-bond network in ice is by Herrero and Ramirez<sup>29</sup> where

Received: April 10, 2021

Published: December 20, 2021



they defined topological densities for ices via parameter  $a$ . The latter gives an overview of the nature of the different H-bond networks, thereby allowing direct comparison between different crystalline ice structures such as the observation of similar topological environments between ices *Ih* and *II*.

Alternatively, a delineation of the H-bonds can also be presented based on the bond strength descriptors obtained from the local vibrational mode (LVM) theory introduced by Konkoli and Cremer.<sup>30–34</sup> They derived LVMs from normal vibrational modes, which generally cannot be used to directly assess the bond strength of a chemical bond/interaction in polyatomic molecules. This shortcoming stems from the delocalization<sup>35,36</sup> of normal vibrational modes and this was addressed in the process of deriving LVMs and the resulting local stretching force constants can be used to measure intrinsic bond strength.<sup>37</sup> The reader is encouraged to refer to a comprehensive review by Kraka et al.<sup>38</sup> on the origin and applications of LVM theory. In essence, LVM analysis has advanced as a powerful analytical tool, extensively applied to a broad range of chemical systems from simple molecular systems to systems in solution<sup>39,40</sup> to proteins<sup>41,42</sup> accounting for both covalent bonds<sup>43–57</sup> and noncovalent interactions<sup>54,58–72</sup> including H-bonds.<sup>73–83</sup> Recently, a whole new scope of chemical systems were unlocked with the extension of LVM theory to periodic systems<sup>84</sup> of one-through three-dimensions, which has enabled us to probe the nature of crystal bonding. A LVM in a periodic system is defined as a vibration driven by a specific internal coordinate in all primitive cells while relaxing all other parts of the periodic system. This approach accommodates a head-to-head comparison of the intrinsic bond strength in periodic and molecular systems. Also, it does not suffer from certain restrictions imposed by periodicity; for example, the lattice structure prevents the calculation of bond dissociation energies or the reduced functionality of some standard analytical tools; for example, periodic NBO<sup>85</sup> does not provide second-order perturbation energies. Due to these superiorities, periodic LVM analysis has already been used as an operating tool to quantify intrinsic bond strengths in materials/crystals; its debut application was focused on analyzing a special type of halogen bonding in crystals.<sup>72</sup>

In this work, we used periodic LVM theory for a deeper understanding of H-bonds in ice crystals which entails a quantification of intrinsic H-bond strengths. The following objectives were pursued in this work.

- To quantify the intrinsic H-bond strength in ice crystals at an individual H-bond scale and discover correlations with geometrical parameters such as H-bond length and angle.
- To clarify and comment on the conventional view whether there is a homogeneous bond strength distribution within ice structures due to the fact that it is a three-dimensional assembly of the same tetracoordinated local H-bond environments.
- To identify and characterize distinct local structural features, that is, rings and different H-bond environments incorporated in those elements, responsible for disparate bond strength distributions in ices.
- To compare different H-bond strengths in different ices.
- To explore the water–ice phase diagram in connection with the variation of H-bond strengths from ambient to high pressures.

The paper is structured as follows: First, a description of Computational Details (Section 2) is provided. In the Results

and Discussion (Section 3), key focus is on determining intrinsic H-bond strength in ices, followed by an analysis of its relation to various local structural features of ice within the global topology of H-bond frameworks. Finally, highlights of this work are emphasized in Conclusions (Section 4), along with a future outlook.

## 2. COMPUTATIONAL DETAILS

In this work, 16 ices were investigated out of 19 different crystalline ice phases that have been identified hitherto in the water–ice phase diagram. These include several hydrogen disorder–order pairs (disordered ice listed first) which are *Ih*<sup>86</sup>–*XI*,<sup>87</sup> *III*–*IX*,<sup>88</sup> *VII*–*VIII*,<sup>89</sup> *V*<sup>90</sup>–*XIII*,<sup>12</sup> *XII*<sup>91</sup>–*XIV*,<sup>12</sup> and *VI*<sup>89</sup>–*XV*.<sup>92</sup> In the case of the latter, new hydrogen-(dis)ordered structures related to ice *VI* were discovered very recently by three independent experimental studies where each were assigned as the 19th ice polymorph, ice *XIX*.<sup>93–95</sup> Here, we considered the weakly ordered ice *XIX* structure determined by Salzmann et al.<sup>93</sup> in our work. In addition, ice *II*<sup>96,97</sup> and metastable ice *IV*<sup>98</sup> were also investigated for which no (dis)ordered counterparts have been identified yet. Another interesting ice crystalline phase we considered is ultralow-density porous ice *XVII*<sup>99</sup> which has its stability domain in the negative pressure regions but metastable at ambient pressures and low temperatures. The modeling of orientationally ordered ice phases is straightforward and initial structures can be obtained via experimental crystal structures, but for the ices with H-disorder, it is important to account for their hydrogen disorder. In practice, this is accomplished by two different means: constructing a large supercell<sup>100,101</sup> or considering a series of possible configurations for a primitive unit cell.<sup>22,102</sup> As our force constant calculations require evaluation of the Hessian matrix and therefore involving a large supercell, particularly as in the case of ice *V* which already has 84 atoms in its primitive unit cell, will lead to an impractical situation challenging the limits of our computational resources. Thus, we adhered to the second approach where different configurations accommodated within a primitive unit cell are considered to incorporate H-disorder. Here, a configuration refers to any distinct way the hydrogen atoms can arrange while keeping the oxygen sublattice intact while obeying the ice rules. To generate different H-oriented configurations, we employed two popular programs based on group and graph theory which are GenIce<sup>103</sup> and Graph Enumeration.<sup>104</sup> The former can be used to generate a set of random configurations starting from a (non-)primitive unit cell, while the latter facilitates the enumeration of all symmetrically distinct configurations that is possible within a given unit cell. Using both methods interchangeably, we generated 50 structures for each H-disordered ice. Single-point calculations were done to obtain total electronic energies, and the configurations were arranged according to their relative energy per H<sub>2</sub>O. Eventually five structures were selected such that their energies are evenly spaced throughout the entire energy range, which corresponded to first, middle, 25, 75%, and last points in the range considered. In addition, we also assessed structures provided in ref 105 as ground-state structures ( $c_0$ ) for some of the H-disordered ices where they used unit cell volume (attributed to a certain mass density) as a most reliable measure of the quality of the structure and likely fixed H-positions to achieve volumes as close as to the experiment. After geometry optimization, these configurations were reordered as  $c_1$ ,  $c_2$ ,  $c_3$ ,  $c_4$ , and  $c_5$ , where  $c_1$  and  $c_5$  represent lowest and highest energy configurations, respectively. As seen from Figure S1 in the

**Table 1.** Calculated Equilibrium Primitive Unit Cell Volumes ( $\text{\AA}^3/\text{H}_2\text{O}$ ), Lattice Energies (kcal/mol), and Equilibrium O–H and  $\text{O}\cdots\text{H}$  Bond Lengths ( $\text{\AA}$ ) for the 16 Ices Calculated at the vdW-DF2 Level

ice	no.	space	lattice	experimental				vdW-DF2					
				polymorph	water	group	system	volume <sup>a</sup>	$E_{\text{lat}}$ <sup>b</sup>	O–H <sup>c</sup>	$\text{O}\cdots\text{H}^c$	volume	$E_{\text{lat}}$
Ih	12	$P6_3/mmc$	hexagonal	32.05	14.07	0.850	1.913	33.18	14.17	0.991	1.793		
II	12	$R\bar{3}$	rhombohedral	24.97	14.05	0.971	1.840	25.82	14.03	0.988	1.841		
III	12	$P4_12_12$	tetragonal	25.69	13.85			26.22	14.05				
IV	16	$R\bar{3}c$	trigonal	23.46				24.17					
V	28	$A2/a$	monoclinic	24.27				24.76					
VI	10	$P4_2/nmc$	tetragonal	22.84	13.68			23.15	13.94				
VII	16	$Pn\bar{3}m$	cubic	20.26	13.07			20.86	13.46				
VIII	8	$I4_1/amd$	tetragonal	20.09	13.31	0.969	1.911	20.88	13.47	0.983	2.023		
IX	12	$P4_12_12$	tetragonal	25.63	13.97	1.004	1.772	26.06	14.21	0.988	1.822		
XI	8	$Cmc2_1$	orthorhombic	31.22		0.992	1.769	33.10		0.991	1.793		
XII	24	$I\bar{4}2d$	tetragonal	23.12				23.64					
XIII	28	$P2_1/a$	monoclinic	23.91		0.975	1.833	24.53	14.08	1.004	1.847		
XIV	12	$P2_12_12_1$	orthorhombic	23.12		0.972	1.845	23.75	14.03	0.987	1.859		
XV	10	$P1$	tetragonal	22.45		1.001	1.863	23.27	13.88	0.986	1.881		
XVII	12	$P6_122$	hexagonal	35.00		1.015	1.747	36.14		0.990	1.804		
XIX	20	$Pbcn$	orthorhombic	19.18				22.73					
							MD		0.22	0.126	0.019		
							MAD		0.32	0.126	0.045		
							MRD (%)	3.8					
							MARD (%)	3.8					

<sup>a</sup>Values taken from refs 12 86,–93 96 98, and 99. <sup>b</sup>Values taken from ref 133. <sup>c</sup>Values taken from refs 12, 15, 88, 89, 92, 134–136.

Supporting Information, relative stabilities yielded for these configurations by both density functionals employed in our work were highly consistent. Furthermore, it should be mentioned that all these configurations vary only within 0.3 kcal/mol·H<sub>2</sub>O at most of each other as revealed by energies of the optimized configurations.

The calculations were carried out with nonlocal dispersion-corrected van der Waals density functional, vdW-DF2,<sup>106</sup> which repeatedly appeared in recent literature as one of the best choices for predicting accurate lattice energies of ices.<sup>28,107–111</sup> For comparison, we computed the same with the CRYSTAL17<sup>112,113</sup> program using the BLYP<sup>114,115</sup> functional with D3 London dispersion correction<sup>116</sup> applied in the Becke–Johnson damping variant<sup>117</sup> [BLYP-D3(BJ)], utilizing an atom-centered Gaussian basis set of double-zeta quality, Pople’s 6-31+G(d,2p) basis set.<sup>118–120</sup> The details and results at the BLYP level are included in the Supporting Information. We should mention here that all the trends observed at the vdW-DF2/projector-augmented wave (PAW) level of theory, which will be discussed in detail in the sections to follow, were correctly recovered by the BLYP-D3(BJ)/6-31+G(d,2p) level of theory (see Figure S2 and Table S2 in the Supporting Information). Because both hybrid density functionals rank favorably in benchmark studies<sup>28,107–111</sup> and thus are deemed as good choices for calculating ice structures, we can confirm in our case that the choice of functional and basis set, other than contributing to the accuracy of the results, does not affect the general conclusions derived in this work.

As for the setup of the periodic system, a primitive cell model was used for the calculations as required by the periodic LVM theory.<sup>84</sup> For the vdW-DF2 functional, calculations were carried out with VASP 5.4.4 package<sup>121,122</sup> with the hardest PAW pseudopotentials<sup>123,124</sup> and a 1000 eV plane-wave basis set cutoff. The Monkhorst–Pack scheme<sup>125</sup> was used to sample the Brillouin zone, and a number of *k* points were chosen so that the spacing in the *k*-point grid in each direction of reciprocal space is

within 0.02–0.04  $\text{\AA}^{-1}$ . Geometry optimization and cell relaxation were carried out with a relatively tight criterion until all forces are less than  $10^{-8}$  eV/ $\text{\AA}$ . With VASP, the energy of an isolated water molecule (water monomer) was calculated within a cubic cell of length 15  $\text{\AA}$  to minimize the interaction with its periodic images. In addition to the water monomer, three other reference systems were calculated with VASP, water dimer [(H<sub>2</sub>O)<sub>2</sub>], water hexamer ring [(H<sub>2</sub>O)<sub>6</sub>], and a model water 2D layer adapted from ref 84. Hessian matrices were computed numerically according to a central-difference formula<sup>126</sup> with a step-size of 0.005  $\text{\AA}$ . All Hessian matrices were evaluated at the  $\Gamma$  point ( $q = 0$ ).<sup>127</sup>

For the statistical analysis presented in Section 3.2.2, a box-and-whisker diagram<sup>128</sup> was used where the distribution of data is represented by a box with two whiskers. The horizontal lines correspond to the minimum and maximum. The bottom and top of the box is defined by first and third quartile of data, Q1 and Q3, respectively, while Q2 indicates the location of the median. The vertical length of the box corresponds to the interquartile range  $QR = Q3 - Q1$ , where lower and upper whisker lengths are defined by  $Q1 - 1.5 \times QR$  and  $Q3 + 1.5 \times QR$ , respectively. Data points lower than  $Q1 - q \times QR$  and higher than  $Q3 + q \times QR$  are considered as outliers, where  $q = 1.5$  (black dots) and  $q = 3.0$  (open dots) define mild and extreme outliers, respectively.

For the local mode analysis along with local stretching force constant calculation, an in-house periodic version of the LModeA program package<sup>129</sup> was used. The primitive cell and other graphical representations of the periodic systems were generated with the VESTA3<sup>130</sup> package.

### 3. RESULTS AND DISCUSSION

**3.1. Equilibrium Volumes and Lattice Energies.** Table 1 reports equilibrium volumes, lattice energies ( $E_{\text{lat}}$  at 0 K), and equilibrium O–H covalent and H-bond  $\text{O}\cdots\text{H}$  bond lengths calculated at the vdW-DF2 level. It can be seen that the vdW-DF2 density functional tends to overestimate equilibrium



volumes, giving mean relative deviation (MRD) and mean absolute relative deviation (MARD) of 3.8% with direct comparison to the experimental volumes. As shown by Murray and Galli<sup>28</sup> and Santra et al.,<sup>107</sup> for ices Ih, II, VIII, IX, XIII, XIV, and XV, the effect of zero-point energies (ZPEs) is an important consideration for equilibrium volumes and tends to increase from low- to high-density ices. Accounting for the two extremes of the densities (high and low) covering ices Ih and VIII, ZPE inclusive volumes based on vdW-DF2 functional were shown to deviate from experimental volumes by 1.5 and 5.8%, respectively,<sup>28</sup> deeming this functional as a reasonable choice for predicting volumes. By comparison to experimental volumes, BLYP-D3 dispersion-corrected density functional in general underestimated the volumes with MRD and MARD of 5.4% (see the Supporting Information), where the deviation is expected to reduce with ZPE inclusion. The two density functionals investigated in this work are comparable to some of the best performing density functionals for predicting volumes, such as D4 dispersion-corrected PBE<sup>131</sup> and BLYP<sup>111</sup> functionals, and vdW inclusive functionals such as optPBE-vdW and PBE0 + vdW<sup>TS</sup>.<sup>107</sup> Furthermore, to evaluate the quality of the structural predictions by each density functional, we compared covalent O–H and H-bond O⋯H lengths with that of the experiment for the H-ordered ices, Ih, II, VIII, IX, XI, XII, XIV, XV, and XVII. Here, it should be clarified that for Ih, which is inherently disordered, the ordered Bernal–Fowler model<sup>132</sup> has been used for structure comparison. For OH covalent bonds, we observed mean deviation (MD) and mean absolute deviation (MAD) of 0.126 Å, with vdW-DF2 and MD and MAD of 0.029 Å with BLYP. In the case of H-bonds, vdW-DF2 predicted bond lengths with MD and MAD of 0.019 and 0.045 Å, respectively, and those associated with BLYP were –0.081 and 0.103 Å, respectively. We also compared our calculated lattice energies with the experimental lattice energies obtained by Whalley<sup>133</sup> for seven ice systems, in which ZPE contributions were removed and the energies were extrapolated to 0 K. To draw insights into the quality of the two density functionals employed here with respect to lattice energies, a subset of the 16 ices, formally known as ICE10 data set is considered, which is often used in benchmark studies.<sup>105,131</sup> We could see MD and MAD of 2.3 kcal/mol (over 10%) for the calculated lattice energies with BLYP, which could be improved using other relatively costly density functionals as shown by Brandenburg et al.<sup>105</sup> in their benchmark study. In our work, using vdW-DF2 density functional, we could obtain improved lattice energies with MD and MAD of 0.2 and 0.3 kcal/mol, respectively, which is less than 3% deviation compared to experimental lattice energies. Because an accurate description of H-bond strength mostly relies on the ability to produce reasonable geometries, and in this connection as reflected by low relative deviations associated with the geometry and lattice energies, vdW-DF2 functional performs satisfactorily well compared with BLYP-D3(BJ) and the discussion that follows adheres to vdW-DF2 results. The important results obtained at the BLYP-D3(BJ) level are highlighted within the Supporting Information.

**3.2. Intrinsic Strength of H-Bonds in Ices.** In the following, H-bond strengths as given by local stretching force constants  $k_n^a$  and the relationship to geometrical parameters are probed for all the ices, followed by a statistical analysis of H-bond strengths and a definition of classification criteria for the same.

**3.2.1. Variation of H-Bond Strengths.** The relationship between local stretching force constants  $k_n^a$  and bond lengths  $r$

for H-bonds and covalent OH bonds are shown in Figures 1 and 2, respectively. A strong correlation is observed between  $k_n^a$  and

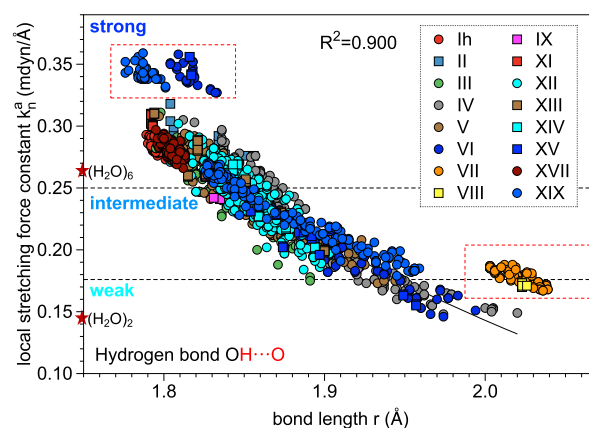


**Figure 1.** Relationship between local stretching force constants  $k_n^a$  and bond lengths  $r$  for H-bonds. Circles and squares distinguish between disordered and ordered ices, respectively, and different colors represent H-bonds in each ice polymorph (refer to inset); within primitive unit cell and across its boundaries. A quadratic function in the form of  $k_n^a = a \cdot r^2 + b \cdot r + c$  was used to fit 1544 data points excluding obvious outlier clusters above  $k_n^a > 0.32$  mdyn/Å and  $r > 2.0$  Å, resulting in  $R^2 = 0.900$ . Outlier clusters are indicated by dashed red boxes. Marked along the y-axis by stars are the  $k_n^a$  values for the reference H-bonds, water dimer [(H<sub>2</sub>O)<sub>2</sub>], and hexamer ring [(H<sub>2</sub>O)<sub>6</sub>]. Dashed horizontal lines correspond to the strength classification in Section 3.2.3.

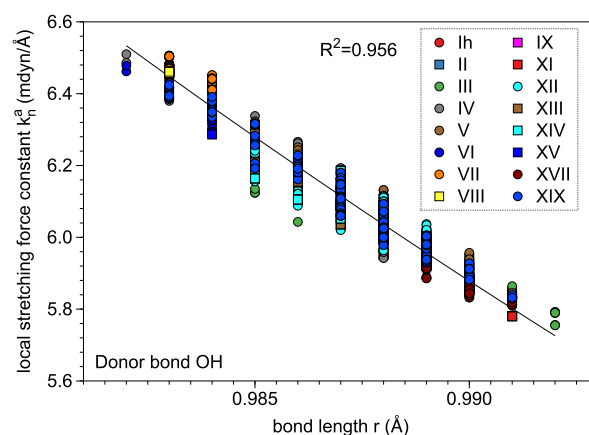


**Figure 2.** Relationship between local stretching force constants  $k_n^a$  and bond lengths  $r$  for OH covalent bonds. Circles and squares distinguish between disordered and ordered ices, respectively, and different colors represent H-bonds in each ice polymorph (refer to inset); within primitive unit cell and across its boundaries. A power function in the form of  $k_n^a = a \cdot r^b$  was used to fit 1792 data points with  $R^2 = 0.956$ .

bond length for OH covalent bonds ( $R^2 = 0.956$ ), whereas that of H-bonds tend to be weaker in comparison ( $R^2 = 0.900$ ). This is a manifestation of the Badger's rule<sup>137,138</sup> for harmonic frequencies and its recent extension to anharmonic frequencies by Xantheas et al.,<sup>139</sup> which in essence states that shorter bonds have larger frequencies (or force constants), thereby yielding stronger bonds. We noticed similar findings were reported in the work by Libowitzky where his work covered a wide range of very weak to strong hydrogen bonds present within various types of minerals.<sup>140</sup> The bond strengths of both H-bond and OH covalent bonds in ices are revealed to vary in a broad range,

0.146–0.359 and 5.755–6.510 mdyn/Å, respectively. While H-bonds in all the ice polymorphs exhibit higher bond strengths than H-bonds in water dimer (0.145 mdyn/Å), only few ices including ice *Ih* have H-bond bond strengths surpassing those of a hexamer water ring (0.269 mdyn/Å), enforced by the *push–pull effect*.<sup>78</sup> On the other hand, in comparison to a model 2D water layer (0.696 mdyn/Å) with highly directional H-bonds,<sup>84</sup> all the ice structures having no such unique orientation of water molecules are bound to have weaker H-bonds.

We also investigated the relationship between the directionality and the H-bond strength, or in other words whether more linear intermolecular H-bonds in ice imply enhanced bond strengths, which is a common phenomenon in proteins<sup>42</sup> and other H-bonded crystals.<sup>141</sup> As deduced from Figure 3, there is a

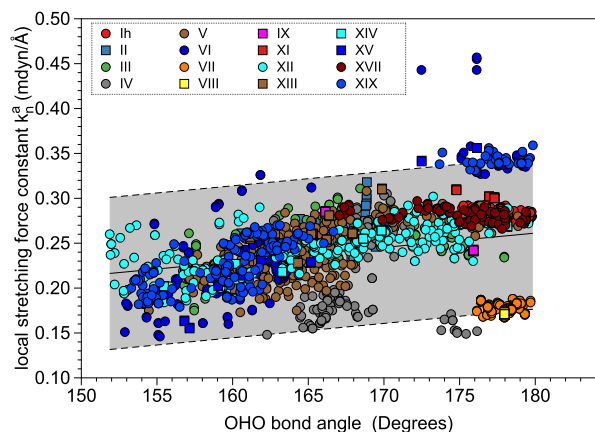


**Figure 3.** Relationship between local stretching force constants  $k_n^a$  and intermolecular OHO angles for H-bonds. The area shaded in gray bounded by dashed lines corresponds to the 95% prediction interval. Circles and squares distinguish between disordered and ordered ices, respectively, and different colors represent OHO angles in each ice polymorph (refer to inset); within primitive unit cell and across its boundaries.

weak correlation between the intermolecular OHO bond angle and  $k_n^a$  as analyzed via a 95% prediction interval which reveals a tendency to show stronger H-bonds with linearization; this is only considering all the ices excluding ices VII and VIII. As for the latter, in spite of having OHO bond angles between 177 and 178°, ices VII and VIII are associated with the weakest H-bonds. One reason could be the repulsion between adjacent O···O contacts within the closely intertwined ice VII/VIII network.

**3.2.2. Distribution of H-Bond Strengths.** A box-and-whisker diagram was employed to analyze the statistical distribution of H-bond strengths in each ice. It can be deduced from Figure 4 that there is a narrow to broad distribution of H-bond strengths considering all the ices. The variation of bond strength distribution can be explained in terms of local structural features of the H-bond topology in each ice, which we will delve into more in detail in Section 3.3. However, a comparison of bond strength distribution between the ices at face value leads to an important result. It can be inferred from the narrow distribution of hexagonal ice *Ih* (or its ordered counterpart ice XI) that the H-bond strengths are more or less evenly distributed throughout its structure, instituting more balance to the H-bond network. This consistency in the bond strengths could be the reason why hexagonal ice is the most prevailing form of ice on earth under ambient conditions.

**3.2.3. Classification of H-Bonds.** A set of classification criteria based on  $k_n^a$  were defined to assign all 1820 H-bonds within the 16 ice polymorphs we investigated into different classes: strong, intermediate, and weak. In line with other theoretical studies that formerly classify ice *Ih* and ice VIII as strong and weak,<sup>27,28</sup> which represent ambient and high pressure ends of the *P–T* phase diagram, we aimed at selecting our criteria such that H-bonds associated with these two ices are assigned entirely weak/strong to be consistent with the above mentioned. Also, the selection was aimed at categorizing H-bonds that can be associated with the same local environment in a particular ice structure, that is, “hex” type rings in ices *Ih*, XI, and II, into the same strength class. This led to the classification of H-bonds as follows:  $\geq 0.250$  mdyn/Å as strong, 0.249–0.177 mdyn/Å as intermediate, and  $\leq 0.176$  mdyn/Å as weak. Figure 5

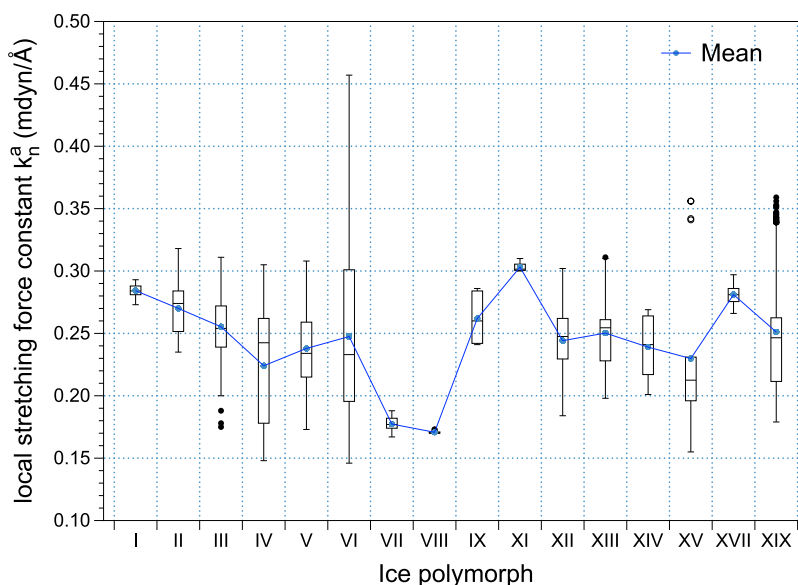


**Figure 4.** Statistical distribution of H-bond strengths in each ice polymorph. The mean (average)  $k_n^a$  value is indicated for each ice with a light blue circle. The solid blue line connecting the mean  $k_n^a$  values is only there to guide the eye.

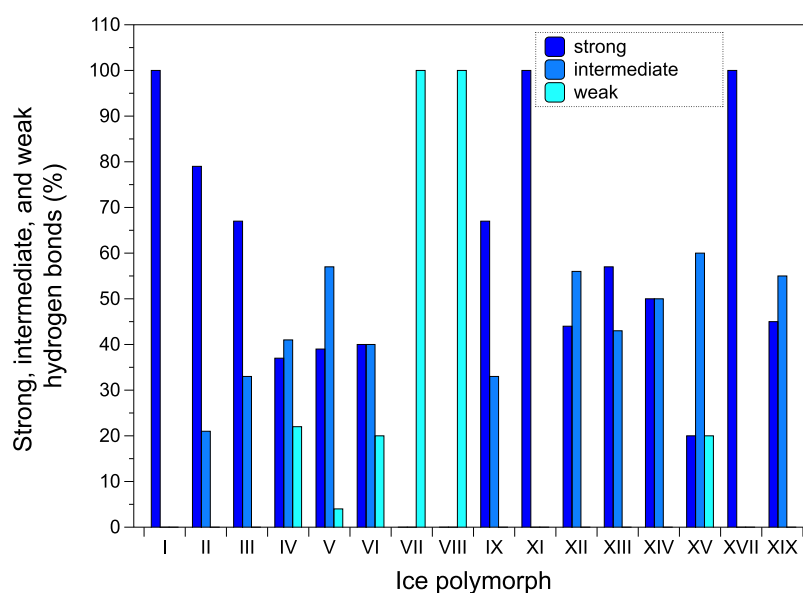


**Figure 5.** Percentage of strong, intermediate, and weak H-bond classes within each ice polymorph represented by differently colored bars. Refer to inset for color representation.

shows the percentage of each type of H-bond present in each of the 16 ice polymorphs. Accordingly, ices *Ih*, XI, and XVII comprise strong H-bonds, and conversely, ices VII and VIII are formed from entirely weak H-bonds. The H-bond networks of ices II, III, IX, XII, XIII, XIV, and XIX correspond to an admixture of strong and intermediate H-bond classes, while all three types of H-bonds are present in ices IV, V, VI, and XV.

**3.3. Local Stretching Force Constant  $k_n^a$  and Local Structural Features of H-Bond Topology of Ices.** As mentioned in Section 3.2.2, the rationale behind the overall trends in the bond strength distribution of ices can be uncovered by focusing on the local details of the structure. In the following, the H-bond networks of each of the 16 ices are discussed with a particular emphasis on identification and characterization of their local structural elements, which cohere to give different topologies to these networks. Table 2 reports average bond lengths  $R_{\text{avg}}$ , average local stretching force constants  $k_{n,\text{avg}}^a$ , and number of H-bonds incorporated in different local structural elements identified within the H-bond networks of each ice. The H-bond networks for the 16 ices are shown in Figures 6–14a with respect to a  $2 \times 2 \times 2$  supercell, where the primitive unit cell is also indicated. Because disordered/ordered ice pairs correspond to the same H-bond topology, H-bond networks and primitive unit cells of only ordered ices are shown. In some cases, noteworthy local structural elements are also presented separately. Different H-bond environments as identified by  $k_n^a$  are distinguished using different colors. The  $2 \times 2 \times 2$  supercell is represented in two ways: (i) each O...O contact around the central water molecule within the local tetrahedral environment is represented by a stick, (ii) water molecules and H-bonds are represented by balls and sticks, and dashed lines, respectively.

In general, up to 0.8 and 9.5% deviations in  $R_{\text{avg}}$  and  $k_{n,\text{avg}}^a$ , respectively, can be seen within the different H-bond environments of H-ordered ices. In the case of H-disordered ices this is even more pronounced. The considerable deviations in  $k_{n,\text{avg}}^a$  in both instances might be caused by numerical errors during the evaluation of the Hessian matrix from numerical differentiation of analytical gradients and also by the large size of primitive unit cells which contain 8–28 water molecules. However, this

precision is sufficient for our purpose of capturing trends in the bond strength variations.

**3.3.1. Ice *Ih*/XI.** Hexagonal ice is a disordered ice phase where the H-bond framework comprises hexagonal rings in chair and boat conformations. The topology of the H-bond network in *Ih* allows for hexagonal channels or chains of cavities which can entrap small atoms such as helium.<sup>142</sup> We probed the hydrogen bond strengths in *Ih* via  $k_n^a$ , and it revealed that the primary structural elements of *Ih*, that is, hexagonal rings, can be associated with the same H-bond environment (Figure 6) which is also true for other high-energy configurations investigated for ice *Ih*. In other words, the H-bond strength in *Ih* is uniformly distributed throughout the framework manifesting a highly balanced H-bond network. The low-temperature ordered counterpart of ice *Ih*, ice XI, exhibited marginally stronger H-bonds.

**3.3.2. Ice II.** Ice II has a fully H-ordered structure composed of puckered hexagonal rings in the [111] direction of the rhombohedral unit cell. The hexagonal rings vary in their degree of puckering leading to flat- and chair-shaped rings. Four types of H-bonds can be identified within the H-bond network of ice II.<sup>143</sup> The H-bonds within the hexagonal rings are referred to as “flat bonds” and “chair bonds”, while those linking hexagonal rings vertically and horizontally are called “pillar” and “bridge” bonds, respectively. In general, ice II structure can be apprehended as a collection of interlinked hexagonal columns, or in other words, “ice nanotubes”.<sup>8</sup> Nakamura et al.<sup>23</sup> determined the hydrogen-bonding energies of these four types of H-bonds using pair interaction energies, and their relative strengths were ranked in the following order: bridge < flat < chair < pillar. We also characterized the bond strengths of these four types of H-bonds, and considering the marginal difference in  $k_{n,\text{avg}}^a$  for “flat” and “chair” bonds, we identified that these hexagonal rings in fact belong to the same H-bond environment which is denoted by type hex. Accordingly, bond strengths in these three different H-bond environments were observed to vary in the order bridge < pillar < hex, and a representation of these bonds within both the H-bond network and a pair of hexagonal columns is shown in Figure 7.

**Table 2.** Average Bond Length Values  $R_{\text{avg}}$  in Å, Average Local Stretching Force Constant Values  $k_{\text{n,avg}}^{\text{a}}$  in mDyn/Å, Each Followed by Respective Standard Deviation Values  $\pm\Delta s$  in Parentheses, and Number of Bonds in Each Environment for Different Local H-Bond Environments, within Primitive Unit Cell and across Its Boundaries, for the 16 Ices Calculated at the vdW-DF2 Level<sup>4a</sup>

type	$R_{\text{avg}} (\pm\Delta s)$						$k_{\text{n,avg}}^{\text{a}} (\pm\Delta s)$						no.
	$c_0$	$c_1$	$c_2$	$c_3$	$c_4$	$c_5$	$c_0$	$c_1$	$c_2$	$c_3$	$c_4$	$c_5$	
	Ice Ih												
hex	1.793 (0.001)	1.797 (0.004)	1.797 (0.004)	1.797 (0.004)	1.798 (0.003)	1.798 (0.003)	0.288 (0.002)	0.284 (0.005)	0.284 (0.004)	0.283 (0.004)	0.283 (0.005)	0.284 (0.003)	24
	Ice XI												
hex	1.793 (0.001)						0.303 (0.004)						16
	Ice II												
hex	1.826 (0.015)						0.288 (0.014)						12
pillar	1.850 (0.003)						0.258 (0.010)						6
bridge	1.863 (0.007)						0.247 (0.015)						6
	Ice III												
helix	1.810 (0.017)	1.822 (0.012)	1.827 (0.021)	1.835 (0.007)	1.845 (0.029)	1.847 (0.042)	0.277 (0.024)	0.266 (0.014)	0.260 (0.022)	0.240 (0.008)	0.234 (0.037)	0.231 (0.046)	8
bridge-1	1.850 (0.009)	1.832 (0.013)	1.823 (0.015)	1.833 (0.019)	1.818 (0.017)	1.839 (0.007)	0.254 (0.017)	0.252 (0.018)	0.265 (0.023)	0.263 (0.028)	0.274 (0.021)	0.253 (0.019)	8
bridge-2	1.824 (0.009)	1.832 (0.013)	1.835 (0.008)	1.820 (0.002)	1.825 (0.014)	1.821 (0.012)	0.254 (0.006)	0.252 (0.018)	0.245 (0.008)	0.256 (0.009)	0.259 (0.022)	0.261 (0.020)	8
	Ice IX												
helix	1.806 (0.000)						0.284 (0.001)						8
bridge-1	1.826 (0.000)						0.260 (0.001)						8
bridge-2	1.835 (0.001)						0.242 (0.001)						8
	Ice IV												
lateral-1		1.840 (0.005)	1.847 (0.014)	1.850 (0.010)	1.849 (0.010)	1.850 (0.003)		0.282 (0.008)	0.273 (0.007)	0.264 (0.017)	0.261 (0.012)	0.266 (0.009)	4
lateral-2		1.854 (0.003)	1.858 (0.014)	1.861 (0.020)	1.856 (0.023)	1.855 (0.015)		0.256 (0.001)	0.255 (0.002)	0.250 (0.016)	0.256 (0.016)	0.262 (0.015)	4
lateral-3		1.833 (0.000)	1.837 (0.009)	1.849 (0.012)	1.849 (0.017)	1.842 (0.001)		0.255 (0.001)	0.271 (0.006)	0.266 (0.014)	0.265 (0.019)	0.260 (0.011)	2
lateral-4		1.868 (0.005)	1.850 (0.016)	1.848 (0.011)	1.852 (0.018)	1.850 (0.027)		0.246 (0.012)	0.262 (0.020)	0.264 (0.012)	0.267 (0.021)	0.262 (0.022)	8
hex-1		1.913 (0.007)	1.931 (0.025)	1.924 (0.036)	1.940 (0.030)	1.927 (0.016)		0.186 (0.004)	0.175 (0.016)	0.185 (0.023)	0.172 (0.016)	0.181 (0.013)	6
hex-2		1.937 (0.001)	1.921 (0.011)	1.955 (0.009)	1.907 (0.023)	1.927 (0.023)		0.173 (0.006)	0.187 (0.011)	0.167 (0.011)	0.192 (0.015)	0.183 (0.013)	4
perpendicular		1.979 (0.000)	1.991 (0.041)	1.991 (0.021)	2.004 (0.000)	2.003 (0.004)		0.164 (0.000)	0.160 (0.016)	0.159 (0.009)	0.151 (0.001)	0.153 (0.000)	2
hex-3		1.958 (0.000)	1.955 (0.006)	1.909 (0.008)	1.922 (0.057)	1.949 (0.005)		0.161 (0.000)	0.172 (0.005)	0.190 (0.001)	0.187 (0.034)	0.171 (0.002)	2
	Ice VII												
cubic	2.021 (0.001)	2.021 (0.018)	2.021 (0.008)	2.020 (0.010)	2.023 (0.003)	2.021 (0.013)	0.175 (0.001)	0.179 (0.007)	0.179 (0.007)	0.178 (0.004)	0.177 (0.002)	0.176 (0.005)	32
	Ice VIII												
cubic	2.023 (0.001)						0.171 (0.001)						16
	Ice V												
octa-1		1.822 (0.012)	1.847 (0.026)	1.833 (0.016)	1.858 (0.023)	1.853 (0.030)		0.267 (0.022)	0.241 (0.032)	0.258 (0.020)	0.230 (0.017)	0.235 (0.025)	8
octa-2		1.844 (0.023)	1.858 (0.025)	1.861 (0.030)	1.861 (0.028)	1.862 (0.032)		0.253 (0.026)	0.237 (0.023)	0.236 (0.028)	0.236 (0.023)	0.233 (0.027)	20
octa-3		1.864 (0.019)	1.861 (0.027)	1.861 (0.038)	1.859 (0.032)	1.850 (0.014)		0.231 (0.016)	0.235 (0.025)	0.238 (0.035)	0.242 (0.034)	0.242 (0.020)	12
octa-4		1.882 (0.028)	1.853 (0.034)	1.869 (0.026)	1.843 (0.024)	1.857 (0.034)		0.218 (0.021)	0.249 (0.033)	0.225 (0.023)	0.257 (0.025)	0.238 (0.030)	8
thread		1.887 (0.026)	1.869 (0.036)	1.872 (0.028)	1.865 (0.030)	1.860 (0.034)		0.211 (0.020)	0.232 (0.032)	0.231 (0.029)	0.229 (0.023)	0.238 (0.038)	8

Table 2. continued

type	$R_{\text{avg}} (\pm \Delta s)$					$l_{\text{n,avg}}^{\text{a}} (\pm \Delta s)$					no.		
	$c_0$	$c_1$	$c_2$	$c_3$	$c_4$	$c_0$	$c_1$	$c_2$	$c_3$	$c_4$		$c_5$	
Ice XIII													
octa-1	1.805 (0.011)						0.285 (0.027)					8	
octa-2	1.828 (0.008)						0.269 (0.014)					20	
octa-3	1.854 (0.004)						0.242 (0.012)					12	
octa-4	1.875 (0.002)						0.229 (0.001)					8	
thread	1.901 (0.001)						0.203 (0.004)					8	
Ice XII													
connect-1		1.855 (0.021)	1.837 (0.004)	1.848 (0.016)	1.859 (0.022)	1.856 (0.016)		0.246 (0.028)	0.265 (0.008)	0.253 (0.017)	0.243 (0.025)	0.244 (0.023)	16
connect-2		1.859 (0.018)	1.844 (0.007)	1.864 (0.023)	1.837 (0.020)	1.843 (0.022)		0.230 (0.019)	0.250 (0.003)	0.227 (0.025)	0.245 (0.015)	0.242 (0.022)	8
zigzag-1		1.847 (0.021)	1.884 (0.020)	1.864 (0.025)	1.861 (0.020)	1.846 (0.024)		0.240 (0.024)	0.209 (0.011)	0.227 (0.026)	0.231 (0.024)	0.245 (0.026)	8
connect-3		1.845 (0.018)	1.833 (0.002)	1.844 (0.012)	1.845 (0.023)	1.857 (0.015)		0.267 (0.017)	0.278 (0.005)	0.266 (0.011)	0.262 (0.019)	0.254 (0.011)	8
zigzag-2		1.853 (0.020)	1.883 (0.011)	1.850 (0.026)	1.848 (0.023)	1.858 (0.014)		0.238 (0.023)	0.207 (0.014)	0.236 (0.027)	0.239 (0.029)	0.234 (0.016)	8
Ice XIV													
connect-1	1.844 (0.002)						0.267 (0.002)						8
connect-2	1.836 (0.000)						0.255 (0.000)						4
zigzag-1	1.859 (0.000)						0.227 (0.000)						4
connect-3	1.876 (0.000)						0.217 (0.001)						4
zigzag-2	1.894 (0.000)						0.202 (0.001)						4
Ice VI													
connect	1.806 (0.002)	1.912 (0.043)	1.858 (0.045)	1.844 (0.045)	1.820 (0.010)	1.883 (0.081)	0.349 (0.002)	0.192 (0.034)	0.273 (0.084)	0.306 (0.070)	0.339 (0.013)	0.257 (0.093)	4
octahed-1	1.844 (0.000)	1.852 (0.006)	1.952 (0.000)	1.908 (0.000)	1.888 (0.033)	1.857 (0.006)	0.254 (0.001)	0.244 (0.006)	0.162 (0.001)	0.212 (0.001)	0.222 (0.017)	0.242 (0.001)	2
octahed-2	1.857 (0.010)	1.897 (0.028)	1.887 (0.049)	1.864 (0.020)	1.866 (0.018)	1.884 (0.047)	0.243 (0.009)	0.216 (0.026)	0.210 (0.038)	0.234 (0.022)	0.235 (0.016)	0.221 (0.036)	4
octahed-3	1.869 (0.000)	1.934 (0.085)	1.887 (0.019)	1.907 (0.006)	1.887 (0.022)	1.863 (0.066)	0.230 (0.001)	0.190 (0.055)	0.209 (0.023)	0.192 (0.014)	0.219 (0.012)	0.266 (0.101)	2
octahed-4	1.920 (0.020)	1.890 (0.065)	1.887 (0.059)	1.902 (0.054)	1.947 (0.037)	1.932 (0.045)	0.190 (0.011)	0.233 (0.083)	0.228 (0.086)	0.214 (0.078)	0.173 (0.021)	0.189 (0.032)	4
octahed-5	1.960 (0.014)	1.838 (0.039)	1.866 (0.032)	1.909 (0.038)	1.908 (0.020)	1.866 (0.039)	0.172 (0.005)	0.300 (0.068)	0.242 (0.066)	0.195 (0.028)	0.194 (0.009)	0.249 (0.061)	4
Ice XV													
connect	1.817 (0.001)						0.349 (0.008)						4
octahed-1	1.854 (0.000)						0.231 (0.000)						2
octahed-2	1.878 (0.009)						0.221 (0.008)						4
octahed-3	1.874 (0.000)						0.203 (0.001)						2
octahed-4	1.895 (0.003)						0.203 (0.008)						4
octahed-5	1.953 (0.005)						0.160 (0.005)						4
Ice XIX													
connect		1.789 (0.005)	1.789 (0.005)	1.786 (0.006)	1.787 (0.001)	1.791 (0.009)		0.343 (0.005)	0.344 (0.006)	0.343 (0.003)	0.339 (0.001)	0.343 (0.010)	8
octahed-1		1.839 (0.008)	1.839 (0.011)	1.841 (0.010)	1.837 (0.008)	1.855 (0.025)		0.255 (0.007)	0.255 (0.010)	0.254 (0.009)	0.256 (0.007)	0.244 (0.019)	10
octahed-2		1.847 (0.015)	1.839 (0.004)	1.847 (0.010)	1.842 (0.006)	1.838 (0.009)		0.248 (0.012)	0.259 (0.009)	0.247 (0.012)	0.255 (0.006)	0.257 (0.006)	4
octahed-3		1.828 (0.000)	1.864 (0.008)	1.837 (0.003)	1.846 (0.004)	1.866 (0.021)		0.270 (0.001)	0.233 (0.004)	0.260 (0.001)	0.250 (0.001)	0.233 (0.004)	2



Table 2. continued

type	$R_{\text{avg}} (\pm \Delta s)$					$k_{n,\text{avg}}^a (\pm \Delta s)$					no.
	$c_0$	$c_1$	$c_2$	$c_3$	$c_4$	$c_0$	$c_1$	$c_2$	$c_3$	$c_4$	
Ice XIX											
octahed-4	1.900 (0.013)	1.887 (0.006)	1.923 (0.022)	1.905 (0.034)	1.885 (0.015)	0.216 (0.009)	0.220 (0.003)	0.200 (0.012)	0.208 (0.017)	0.220 (0.006)	4
octahed-5	1.924 (0.025)	1.919 (0.009)	1.922 (0.032)	1.916 (0.016)	1.910 (0.036)	0.204 (0.012)	0.204 (0.006)	0.201 (0.016)	0.206 (0.015)	0.203 (0.018)	9
octahed-6	1.937 (0.012)	1.949 (0.007)	1.912 (0.033)	1.956 (0.000)	1.924 (0.028)	0.191 (0.005)	0.191 (0.007)	0.210 (0.019)	0.183 (0.000)	0.204 (0.013)	3
Ice XVII											
cage	1.804 (0.004)	1.805 (0.006)	1.804 (0.003)	1.804 (0.005)	1.805 (0.005)	0.280 (0.005)	0.282 (0.007)	0.283 (0.007)	0.282 (0.008)	0.279 (0.005)	24
references					R						$k_n^a$
H <sub>2</sub> O: O–H					0.969						7.563
(H <sub>2</sub> O) <sub>2</sub> : OH...O					2.003						0.145
(H <sub>2</sub> O) <sub>6</sub> : OH...O					1.792						0.269
2D H <sub>2</sub> O <sup>b</sup> : OH...O					2.029						0.696

<sup>a</sup>For each disordered ice, five/six configurations are given and their labeling is according to Section 2. <sup>b</sup>See ref 84.

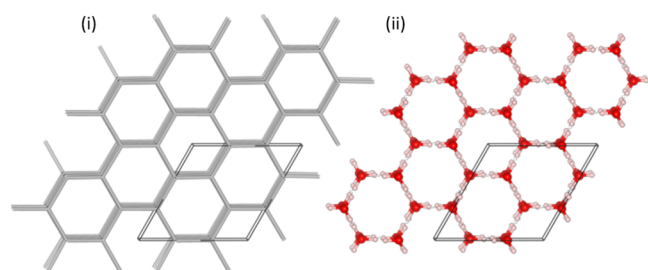


Figure 6. H-bond network of ice Ih.

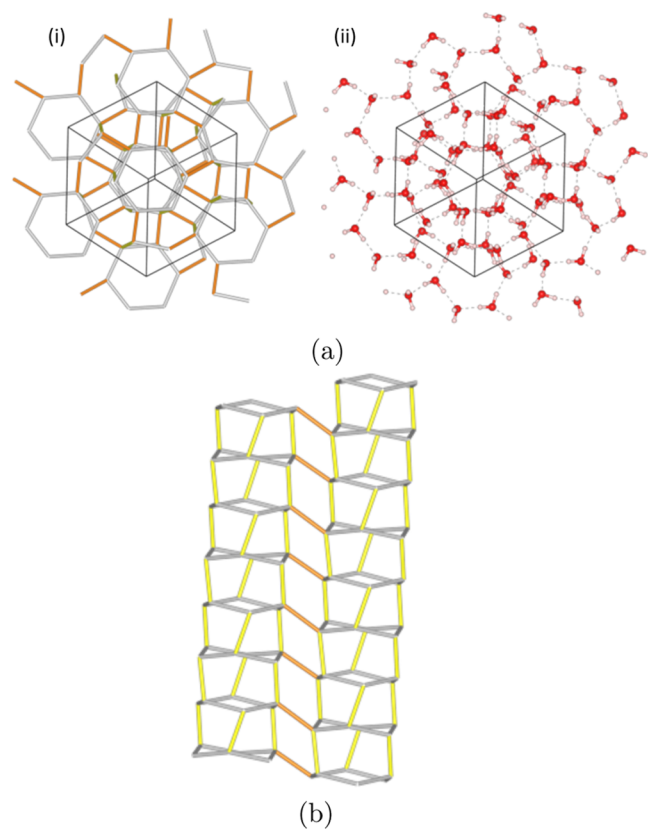


Figure 7. (a) H-bond network of ice II. Different H-bond environments are highlighted as hex (gray), pillar (yellow), and bridge (orange). (b) Side view of a pair of hexagonal columns in ice II.

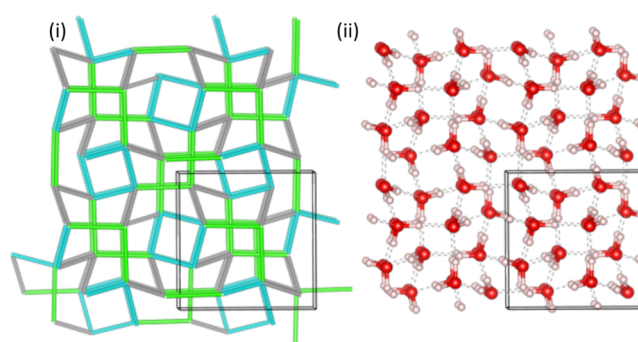
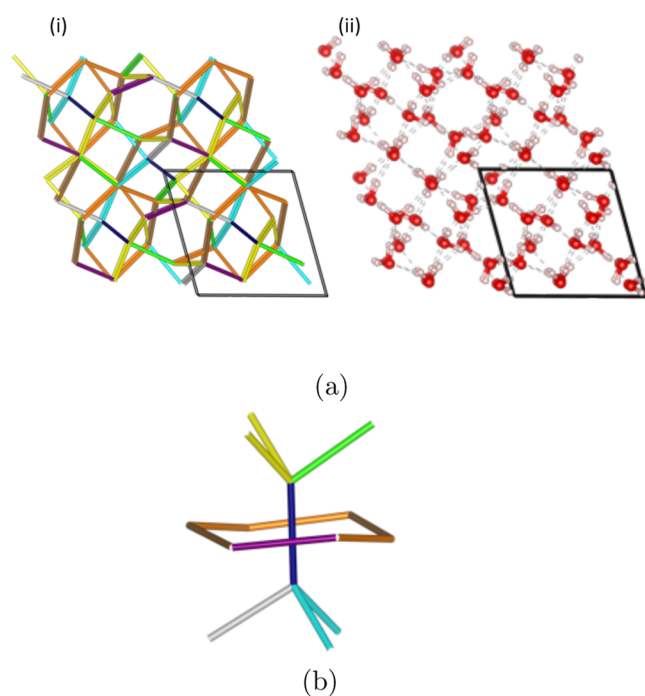


Figure 8. H-bond network of ice IX(III). Different H-bond environments are highlighted as helix (cyan), bridge-1 (green), and bridge-2 (gray).

3.3.3. *Ice III/IX*. Ice IX has an almost completely H-ordered structure with a complex arrangement of five-membered rings in a tetragonal unit cell, and its disordered counterpart is ice III. The structure contains two types of water molecules with oxygen atoms distinguished as O(1) and O(2).<sup>9,144</sup> The topology of the H-bonded network is such that water molecules with atoms O(1) form helices along the *c*-axis and water molecules with atoms O(2) connect adjacent helices. By utilizing  $k_n^a$ , we could identify three types of H-bonds in total; one type corresponding to those connecting O(1)-containing water molecules to each other along with two other different types of H-bonds that connect O(1)-containing water molecules to those of O(2). In other words, the first type of H-bonds connect the water molecules forming the helices, and second and third types bridge those helices into a united framework. Referring to Figure 8 and Table 2, these three types of H-bonds termed as helix (in cyan), bridge-1 (in green), and bridge-2 (in gray) are found to have varying strengths in the order bridge-2 < bridge-1 < helix, as observed for both ices III and IX. Among the other high-energy structures investigated for ice III, only one configuration corresponding to the most stable structure is consistent with the H-bond strength variation of the ground state ( $c_0$  configuration) of ice III and ice IX. The other configurations tend to have at least one of the bridge bonds as the strongest H-bond.

3.3.4. *Ice IV*. A striking feature in ice IV is its self-interpenetrating H-bond network where a single network is



**Figure 9.** (a) H-bond network of ice IV. Different H-bond environments are highlighted as lateral-1 (cyan), lateral-2 (green), lateral-3 (gray), lateral-4 (yellow), hex-1 (orange), hex-2 (brown), hex-3 (purple), and perpendicular (dark blue). (b) Local structure showing hexagonal ring and H-bond through the ring center. In this perspective of a hexagonal ring, each hex-3 (brown) connects two hex-1 (orange) edges of the same type and two edges hex-1 (orange) and hex-3 (purple) of different types.

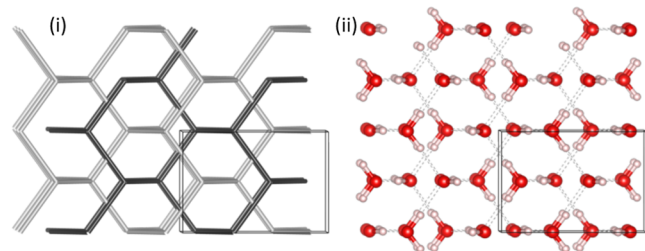


**Figure 10.** H-bond network of ice VIII(VII). Two independent Ic networks termed as cubic are highlighted by gray and dark gray.

present all over the structure. There are two types of crystallographically distinct O atoms, O(1) and O(2), where O(1)-type atoms give rise to puckered six-membered rings.<sup>98</sup> The O(2)-type atoms are H-bonded to each other and run through the center of these six-membered rings and together they form the local structural motif of ice IV. The outward linkage of the latter to other structural motifs fashions a three-dimensional H-bond network in ice IV. According to our H-bond strength analysis and in reference to low-energy  $c_1$  configuration, the lateral H-bonds which extend from O(2)-type atoms to O(1) type atoms, thereby linking three six-membered rings of separate motifs, are the strongest type of H-bonds existing within ice IV. Their strengths vary in the order lateral-1 > lateral-2 > lateral-3 > lateral-4. The six-membered ring entity of the local structure consists of three types of H-bonds, namely, hex-1, hex-2, and hex-3, strength decreasing in the order mentioned and these bonds are weaker than lateral H-bonds, hex-3 being the overall weakest type of H-bond. The

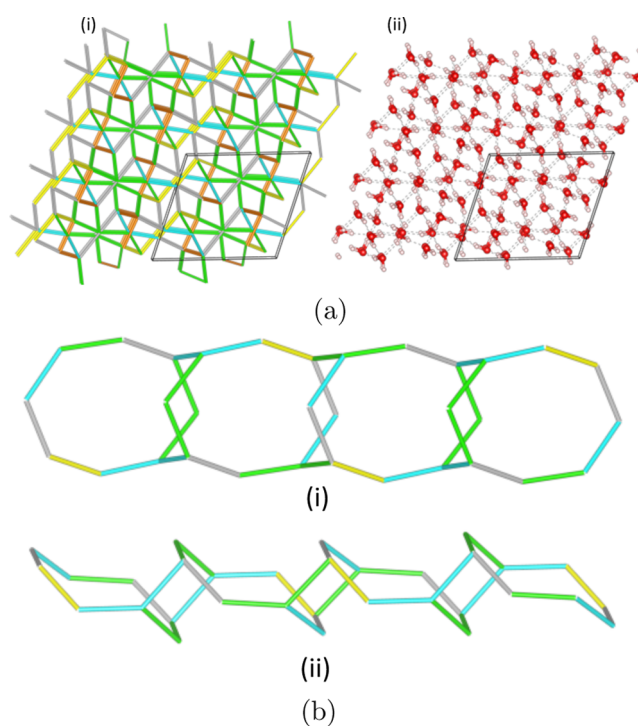


**Figure 11.** (a) H-bond network of ice XIII(V). Different H-bond environments are highlighted as octa-1 (cyan), octa-2 (green), octa-3 (gray), octa-4 (yellow), and thread (orange). (b) Fused eight-membered rings: (i) top view and (ii) side view.

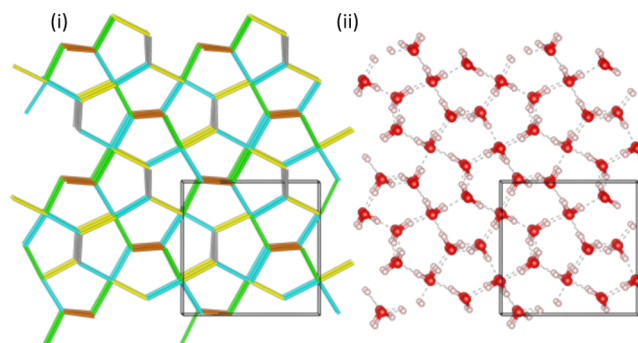


**Figure 12.** H-bond network of ice XIV(XII). Different H-bond environments are highlighted as connect-1 (cyan), connect-2 (green), zigzag-1 (gray), connect-3 (yellow), and zigzag-2 (orange).

second weakest type of H-bonds found within ice IV are termed as perpendicular-type H-bonds, and as mentioned earlier, they correspond to H-bonds running through the center of the six-rings connecting O(2)-type atoms together. This perpendicular H-bond type can be compared to thread-type H-bonds that go through the center of eight-membered rings of the ice V/XIII structure (see Section 3.3.6) in a similar fashion, and those in ice IV are comparatively weaker. The other high-energy configurations considered for ice IV have overall inconsistent bond strength variations yet preserve the strength order where lateral > hex-type H-bonds. In addition, it is observed that perpendicular-type H-bonds tend to be the weakest in these energetically high configurations.

**3.3.5. Ice VII/VIII.** Ices VII/VIII are composed of two independent and interpenetrating networks, each corresponding to the ice Ic structure. Networks with these attributes are recognized as catenated or self-clathrate frameworks, where two

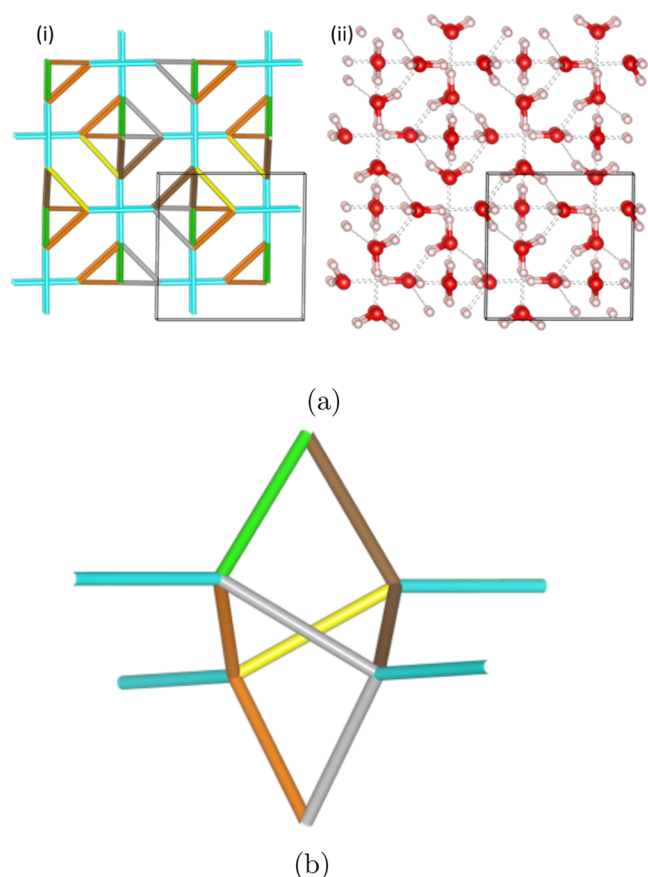


**Figure 13.** (a) H-bond network of ice XV(VI). Different H-bond environments are highlighted as connect (cyan), octahed-1 (green), octahed-2 (gray), octahed-3 (yellow), octahed-4 (orange), and octahed-5 (brown). (b) A distorted octahedron.

identical frameworks are inserted into each other with no H-bonds between the molecules that make up either framework. Similar to hexagonal ice, a uniform bond strength distribution can be identified both within ground and high-energy configurations inspected for ices VII/VIII, pertaining to Ic structural elements. This is termed as cubic H-bond type and depicted in Figure 10. In comparison to the hex-type H-bonds that constitute the hexagonal rings of ices Ih/XI, cubic-type H-bonds in ices VII/VIII are much weaker.

**3.3.6. Ice V/XIII.** The H-bond network in ice V/XIII is the most complicated among known ices and a lucid description of its distinct local features is not so straightforward. It can be perceived as a self-entangled network<sup>13</sup> constituted of bands of fused eight-membered rings with H-bonded chains threading through these rings. Varying ring sizes of four-, five-, six-, and eight-membered rings are present within this framework. We could identify five different H-bond environments, as depicted in Figure 11. The H-bonds, octa-1, octa-2, octa-3, and octa-4, which have decreasing bond strengths in the order mentioned, comprise eight-membered fused rings (Figure 11b), and in fact, octa-1- and octa-2-type strong bonds combine these rings together. Meanwhile, the thread-type H-bonds which have the lowest bond strengths are only visible within the threads that shoot through eight-membered rings and besides thread-type bonds octa- $n$  ( $n = 2, 3, 4$ )-type bonds also merge to form these threads. In the case of disordered ice V structure, the lowest energy conformation ( $c_1$ ) displayed H-bond strength variations in agreement with the ice XIII ordered structure. In comparison

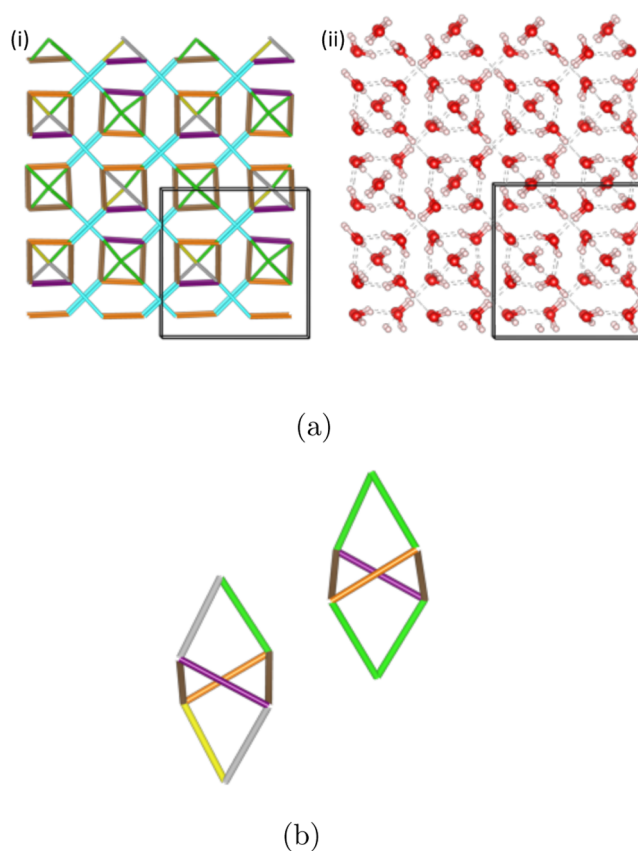


**Figure 14.** (a) H-bond network of ice XIX(VI). Different H-bond environments are highlighted as connect (cyan), octahed-1 (green), octahed-2 (gray), octahed-3 (yellow), octahed-4 (orange), octahed-5 (brown), and octahed-6 (purple). (b) A distorted pair of octahedrons.

to the latter, a weakening of octa-1- and octa-2-type H-bonds along with a strengthening of thread-type bonds can be associated with other high-energy structures of ice V.

**3.3.7. Ice XII/XIV.** This is one of the densest<sup>91</sup> ice forms among those with a simple H-bond topology without any interposition of structural elements. Three crystallographically different molecules<sup>12</sup> exist within this network, corresponding to five different types of H-bond strengths, as revealed by  $k_n^a$ . As highlighted in Figure 12 in gray and orange, two types of H-bonds form “zigzag” chains along the  $c$ -axis of the tetragonal unit cell, while the other three types of H-bonds indicated by cyan, green, and yellow connect these chains together, furnishing a three-dimensional H-bond network. Their bond strengths tend to vary in the order connect-1 < connect-2 < zigzag-1 < connect-3 < zigzag-2. Though it is implied from this particular projection that five- or six-membered rings could be present, in actuality, only seven- or eight-membered rings are present within this framework. Within the representative configurations we considered for disordered ice XII, none of the configurations could produce a H-bond strength variation similar to its ordered counterpart. For the larger part, this might be caused by the deviation of those configurations from the true ground state of ice XII, where the lowest energy conformation is about 3 kcal/mol·H<sub>2</sub>O higher in energy than ordered ice XIV structure. Interestingly, all the high-energy configurations considered here seem to favor connect-3 type as their strongest H-bond.

**3.3.8. Ice VI/XV/XIX.** The H-bond topology of this network also corresponds to the interpenetration of two identical networks with no H-bonds in between, as seen in the ice VI/



VIII framework. The structural element of the VI/XV network resembles a distorted octahedron, made up of six water molecules occupying the vertices of the octahedron, with only eight H-bonds between the vertices. Each distorted octahedron is associated with five different H-bond environments as indicated in Figure 14a as octahed- $n$  ( $n = 1, 2, 3, 4, 5$ ), whereas the H-bonds termed as connect, which also turn out to be the strongest, link these octahedrons together. This trend is also true for the ice VI ground-state structure, although other high-energy configurations of ice VI diverge from this result, lowest energy configuration being about 0.04 kcal/mol·H<sub>2</sub>O higher than the ground state. There is no consensus among these high-energy configurations with regard to H-bond strength variation.

Another very recently discovered and what was determined to be a very weakly hydrogen ordered phase of ice VI is ice XIX.<sup>93</sup> The latter is created via mechanical distortion of the local structure of ice VI, that is, octahedra or in other words hexameric units, under pressure.<sup>93</sup> Interestingly, one of the high-energy configurations ( $c_4$ ) examined for ice XIX, lying about 0.2 kcal/mol·H<sub>2</sub>O above the ground state of ice VI ( $c_0$ ), turned out to possess bond strength variations conforming to those in ices VI and XV. Compared to ice XV, an additional H-bond environment is present within ice XIX giving rise to two different types of octahedra. The growing complexity of the H-bond network can be well understood in connection with the structure. As mentioned before, ice XIX is derived from a distortion of the local structure (octahedra) of ice VI.

**3.3.9. Ice XVII.** Low-density porous ices, which have densities lower than ice XI, have drawn much attention both in a practical aspect as an efficient medium for hydrogen storage as well as in a theoretical aspect, as their stability regions extend the water–ice phase diagram into the negative pressure regime. In their work, del Rosso and co-workers<sup>99</sup> derived ice XVII, a guest-free crystalline ice phase by emptying guest atoms/molecules enclosed in the cavities of a hydrogen hydrate or otherwise known as ice clathrate. This new form of ice was demonstrated to be metastable at room pressure below 120 K. According to our H-bond strength characterization, ice XVII is composed of cages, comparable in strength to ice Ih and XI (Figure 15).

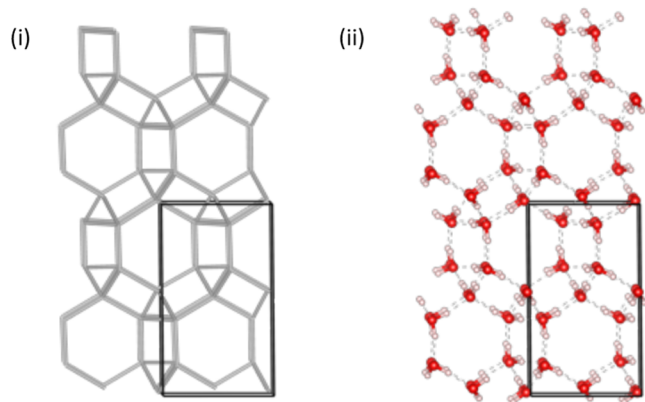


Figure 15. H-bond network of ice XVII.

**3.3.10. Push–Pull Effect in Ice Lattices and Intrinsic Strength of the Local Structure.** Overall, our study clearly reveals that the majority of the ices are composed of different types of H-bonds with varying strengths. In the case of ices Ih and VIII (VII), only one type of H-bond is present within the H-bond network of each ice, termed as hex and cubic types,

respectively. Although both types of bonds are arranged in a six-membered ring, it is interesting to see the striking difference between their bond strengths where hex type in ices Ih (XI) is significantly stronger than cubic type in ices VIII (VII) by about 0.113 (0.132) mdyne/Å. This could be a direct consequence of the topology of the H-bond network, which corresponds to the interposition of two identical Ic networks in the case of ice VIII (VII). In this setting, the repulsive nature between the oxygen atoms in close proximity leads to the weakening of the cubic-type bonds. Apart from the mentioned, all other ices accommodate different types of H-bonds in their framework, which could be somewhat counterintuitive given the fact that all the ices originate from the same local tetracoordinated environment. This is due to the fact that according to the Bernal–Fowler ice rules, the arrangement of these local environments gives rise to different local structural elements which in turn can be attributed to different H-bond strengths.

In addition, it is of interest to inquire the underlying physical phenomenon that contributes to the different bond strengths in various types of H-bonds within a particular ice. As shown by Tao et al.<sup>77</sup> in their investigation of different H-bond types in water clusters, when a donor and an acceptor water molecule participating in a H-bond simultaneously accepts from and donates to other peripheral water molecules, the target H-bond is strengthened by the so called *push–pull effect*. The ideal situation is where the donor molecule accepts two peripheral water molecules which pulls electron density from the donor, meanwhile where the acceptor donates to two peripheral water molecules which pushes electron density toward the acceptor. This synchronized effect ultimately leads to a directional high polarization of the target H-bond. In analogy to H-bonds in ice, this optimal situation is perturbed where the donor and acceptor can donate and accept an additional H-bond as dictated by the tetragonal coordination. In principle, when this perturbation significantly changes the directionality of the *push–pull effect*, the bond-strength of the target H-bond undergoes substantial changes. We tested this hypothesis by comparing the *push–pull* setting for different H-bond types in ice II as a case study.

Figure 16 depicts the directionality of the *push–pull effect* that can be observed in a typical setting for a hex, pillar, and bridge H-bond in ice II. The black arrows indicate the same directionality of the *push–pull effect*, while dashed red arrows highlight the deviations from the said direction. The peripheral water molecules that are responsible for these deviations are marked as  $P_x$  and  $P_y$ , and we monitored angles  $P_xDA$  and  $P_yAD$  with donor (D) and acceptor (A) water molecules of the target bond for the three types of H-bonds. In comparison to both hex and pillar, the bridge-type H-bond corresponds to angles which are more in-plane ( $125.5$  and  $126.9^\circ$ ) with D and A water molecules. In contrast, for both hex- and pillar-type H-bonds, one of the angles leading to the deviations is out-of-plane ( $85.0$  and  $85.4^\circ$ ). Thus, it can be deduced that in the case of bridge-type H-bonds, the in-plane angles lead to a higher perturbation in the *push–pull* direction, thereby weakening the target H-bond. On the other hand, when the peripheral water molecules supporting the *push–pull* direction are associated with more in-plane angles, the consequent *push–pull effect* is high, which is reflected in higher bond strengths. As compared for pillar and hex types, the latter corresponds to more in-plane angles that are close to  $120^\circ$ , and the enhanced *push–pull effect* in this situation results in stronger hex-type bonds.

**3.4. Local Stretching Force Constant  $k_H^0$  and Water–Ice Phase Diagram.** The water–ice phase diagram presents the



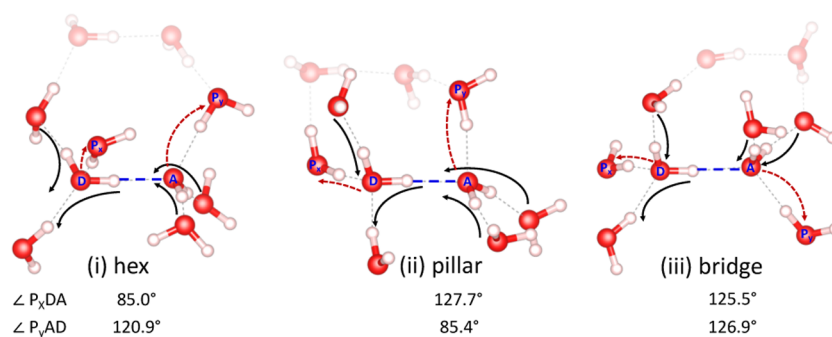


**Figure 16.** Schematic of the *push–pull effect* for the hex-, pillar-, and bridge-type bonds in ice II. The target H-bond between the donor (D) and acceptor (A) water molecules is marked in blue where dotted black lines show the H-bonds with peripheral water molecules. The adjacent water molecules are in transparent. The direction of the *push* or *pull* is indicated by black arrows and dashed red arrows indicate those which deviate from that direction. The angles between the peripheral water molecules,  $P_x$  and  $P_y$ , and D and A water molecules are given by  $P_xDA$  and  $P_yAD$ .

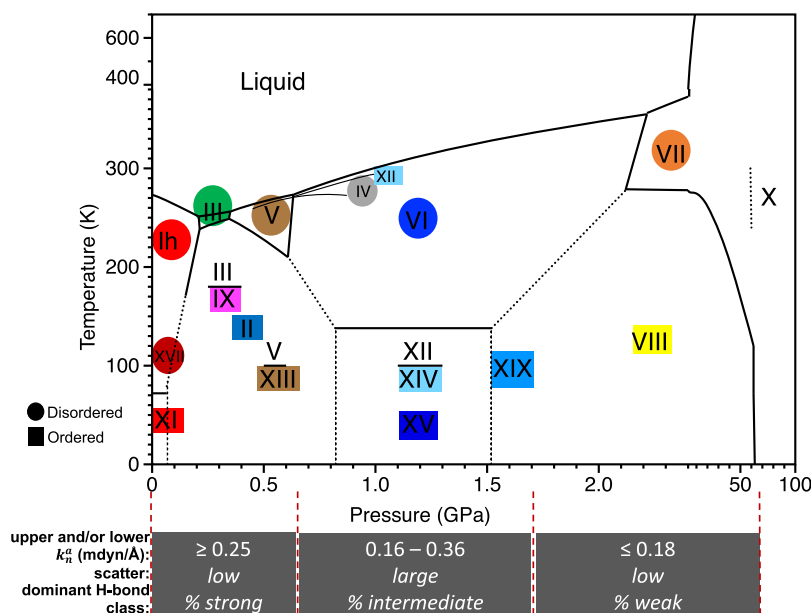


**Figure 17.** H-bond strength variation across the water–ice phase diagram. Gray bars in the bottom, spanning three pressure regions (0–0.7, 0.7–1.6, and 1.6–50 GPa), indicate upper and/or lower boundaries of  $k_n^a$  values, followed by the nature of scattering of  $k_n^a$  values and dominating H-bond class. The latter is obtained via considering higher percentage of strong, intermediate, or weak H-bond class for ices included within a particular pressure region. Circles and squares distinguish between disordered and ordered ices, respectively, and colors for indicating different ices are consistent with Figures 1–3.

domains of stability for known and predicted ices in the phase range up to 100 GPa. Several experimental and/or computational investigations have led to the determination of phase boundaries between ices *Ih*, II, III, V, VI, and VII and water, while fields of stability for some ices such as ices XIII and XIV have not been established yet. Ices *Ic*, IV, IX, and XII are metastable because they do not have their own regions of stability but exist in the stability range of another ice phase. The newest additions to the water–ice phase diagram are ices XVII and XIX, and the former is distinctive as it extends stability regions of the phase diagram to the negative pressure ends as well. Thermodynamically stable ices can also exist beyond their fields of stability, but preferentially transforms to the most stable form under that  $P$ – $T$  conditions, that is, most high-pressure ices are metastable at ambient pressures and slowly transform to *Ih*. Exploration of the water–ice phase diagram has many facets; it can be analyzed in a thermodynamic aspect to obtain information about phase transitions and equations of state for coexisting phases<sup>145</sup> or can be studied for its chemical

dimensions such as the influence by acid/base dopants on H-ordering processes,<sup>8</sup> or the focus can be on extreme conditions such as terapascal (TPa) pressure regimes which extend our understanding on morphology and evolution of ice giants in the solar system.<sup>146</sup>

An alternative route to traverse the water–ice phase diagram is to monitor the variation of lattice energies across the different ice phases. The experimental lattice energies by Whalley,<sup>133</sup> which extrapolate phase coexistence lines measured at finite temperature and pressure to zero temperature and pressure, have been utilized to compare the stability of ices.<sup>147</sup> As the lattice energy reflects the collective H-bond strengths of the H-bond network of a particular ice polymorph, we examined its variation across the phase diagram moving from ambient to high pressures based on the calculated lattice energies in this work. We could observe moving from left to right in the phase diagram that for ices with unambiguously defined phase boundaries, the corresponding calculated lattice energies decreased in the order *Ih* > III > II > VI > XV > VIII > VII. Not so surprisingly, we could

see this trend duly reflected in the subsequent analysis based on the characterization of the H-bond network via  $k_n^a$ , which is explained in detail below.

As shown in Figure 17, the ices within gradually increasing pressure regimes of the phase diagram are associated with their dominating H-bond classes based on our strong, intermediate, and weak classification presented in Section 3.2.3. Accordingly, ices Ih, II, III, IX, XIII, and XVII which can be found in the 0–0.7 GPa region of the phase diagram are dominated by strong H-bonds with a low scattering of bond strength values, latter higher than 0.25 mdyne/Å. The ices in the central region of the phase diagram (0.7–1.6 GPa) have a high percentage of intermediate H-bonds, with the largest scattering of bond strength values, varying between 0.16 and 0.36 mdyne/Å. The ices VII and VIII in the very high pressure end of the phase diagram (up to 50 GPa) mostly comprise weak H-bonds. Thus, going from left to right in the phase diagram, the predominant class of bond strengths associated with different H-bond network topologies of ices vary from strong to weak. Consequently, increasing pressures are required in order to stabilize these ices. Reverting to the similar trend observed with lattice energies, this is a confirmation that H-bond strength measured via  $k_n^a$  can correctly capture the binding energy between water molecules as collectively measured via lattice energy. Furthermore, as  $k_n^a$  calculation does not impose pressure, it can exclusively characterize the pure electronic effects of H-bonding in ice.

#### 4. CONCLUSIONS

Herein, we employed the extension of the LVM theory to solid-state systems to characterize H-bonds in several ice crystals. The local environment in the H-bond network of ice corresponds to a tetrahedral coordination at each water molecule, and the global topology of ice can be perceived to emerge from the integration of these similar sites according to the Bernal–Fowler ice rules. Due to this uniformity in the ice structure, one would expect to see a homogeneous H-bond strength distribution within ices which can ideally be quantified via one bond strength value as attempted in ref 148; we could clarify in this work that this is not the case. Based on the assessment of the intrinsic H-bond strength within 16 ices we investigated, we could observe an array of bond strength distributions. Apart from hexagonal ice, frequently occurring form of ice on the earth's surface, and ice VIII(VII), existing in the earth's interior, both of which displayed a uniform distribution of H-bond strengths as quantified via  $k_n^a$ , all the other ices exhibited disparate bond strength distributions. We could explain these broad bond strength distributions in terms of different local structural elements embedded within the H-bond framework of each ice. Different H-bond types with varying strengths can be associated with these elements and hence the disparity. The bond strengths in different H-bond types in a particular ice are governed by the *push–pull effect*. Moreover, based on the strong, intermediate, and weak H-bond classification presented in this work, we could shed light on the H-bond strength variation across the water–ice phase diagram. In summary, these new findings on the H-bond strengths of the known ices provide important new guidelines with regard to the verification of the existence of different H-bond networks, bolstering research in novel ice structure prediction.

#### ■ ASSOCIATED CONTENT

##### Supporting Information

The Supporting Information is available free of charge at <https://pubs.acs.org/doi/10.1021/acs.jctc.1c00357>.

Local mode properties of H-bonds and donor OH bonds of the ICE10 set calculated at BLYP and vdW-DF2 levels and peripheral angles supporting the *push–pull* effect in a typical setting of different H-bond types in ice II (PDF)

Optimized geometries in fractional coordinates and primitive unit cell parameters for 16 ices calculated at the vdW-DF2 level and ICE10 set at the BLYP-D3(BJ)/6-31+G(d,2p) level (ZIP)

#### ■ AUTHOR INFORMATION

##### Corresponding Author

Elfi Kraka – *Computational and Theoretical Chemistry Group (CATCO), Department of Chemistry, Southern Methodist University, Dallas, Texas 75275-0314, United States;*

orcid.org/0000-0002-9658-5626; Email: [elfikraka@smu.edu](mailto:elfikraka@smu.edu)

##### Authors

Sadisha Nanayakkara – *Computational and Theoretical Chemistry Group (CATCO), Department of Chemistry, Southern Methodist University, Dallas, Texas 75275-0314, United States*

Yunwen Tao – *Computational and Theoretical Chemistry Group (CATCO), Department of Chemistry, Southern Methodist University, Dallas, Texas 75275-0314, United States*

Complete contact information is available at: <https://pubs.acs.org/10.1021/acs.jctc.1c00357>

##### Author Contributions

<sup>†</sup>S.N. and Y.T. contributed equally to this work.

##### Notes

The authors declare no competing financial interest.

#### ■ ACKNOWLEDGMENTS

This work was supported by the National Science Foundation (grant CHE 2102461). The authors thank Southern Methodist University for providing excellent computational resources.

#### ■ REFERENCES

- (1) Cleaves, L. I.; Bergin, E. A.; Alexander, C. M. O. D.; Du, F.; Öberg, K. I.; Harries, T. J. The Ancient heritage of Water Ice in the Solar System. *Science* **2014**, *345*, 1590.
- (2) Filacchione, G.; De Sanctis, M. C.; Capaccioni, F.; Raponi, A.; Tosi, F.; Ciarniello, M.; Cerroni, P.; Piccioni, G.; Capria, M. T.; Palomba, E.; Bellucci, G.; Erard, S.; Bockelee-Morvan, D.; Leyrat, C.; Arnold, G.; Barucci, M. A.; Fulchignoni, M.; Schmitt, B.; Quirico, E.; Jaumann, R.; Stephan, K.; Longobardo, A.; Mennella, V.; Migliorini, A.; Ammannito, E.; Benkhoff, J.; Bibring, J. P.; Blecka, M. I.; Carlson, R.; Carsenty, U.; Colangeli, L.; Combes, M.; Combi, M.; Crovisier, J.; Drossart, P.; Encrenaz, T.; Federico, C.; Fink, U.; Fonti, S.; Ip, W. H.; Irwin, P.; Kuehrt, E.; Langevin, Y.; Magni, G.; McCord, T.; Moroz, L.; Mottola, S.; Orofino, V.; Schade, U.; Taylor, F.; Tiphene, D.; Tozzi, G. P.; Beck, P.; Biver, N.; Bonal, L.; Combe, J.-P.; Despan, D.; Flamini, E.; Formisano, M.; Fornasier, S.; Frigeri, A.; Grassi, D.; Gudipati, M. S.; Kappel, D.; Mancarella, F.; Markus, K.; Merlin, F.; Orosei, R.; Rinaldi, G.; Cartacci, M.; Cicchetti, A.; Giuppi, S.; Hello, Y.; Henry, F.; Jacquino, S.; Reess, J. M.; Noschese, R.; Politi, R.; Peter, G. Exposed

Water Ice on the Nucleus of Comet 67P/Churyumov–Gerasimenko. *Nature* **2016**, *529*, 368–372.

(3) Lis, D. C.; Bockelée-Morvan, D.; Güsten, R.; Biver, N.; Stutzki, J.; Delorme, Y.; Durán, C.; Wiesemeyer, H.; Okada, Y. Terrestrial Deuterium-to-hydrogen Ratio in Water in Hyperactive Comets. *Astron. Astrophys.* **2019**, *625*, L5.

(4) Li, S.; Lucey, P. G.; Milliken, R. E.; Hayne, P. O.; Fisher, E.; Williams, J.-P.; Hurley, D. M.; Elphic, R. C. Direct Evidence of Surface Exposed Water Ice in the Lunar Polar Regions. *Proc. Natl. Acad. Sci. U.S.A.* **2018**, *115*, 8907–8912.

(5) Tielens, A. G. G. M.; Hagen, W.; Greenberg, J. M. Interstellar Ice. *J. Phys. Chem.* **1983**, *87*, 4220–4229.

(6) Gibb, E. L.; Whittet, D. C. B.; Boogert, A. C. A.; Tielens, A. G. G. M. Interstellar Ice: The Infrared Space Observatory Legacy. *Astrophys. J., Suppl. Ser.* **2004**, *151*, 35–73.

(7) Boogert, A. C. A.; Gerakines, P. A.; Whittet, D. C. B. Observations of the Icy Universe. *Annu. Rev. Astron. Astrophys.* **2015**, *53*, 541–581.

(8) Salzmann, C. G. Advances in the Experimental Exploration of Water's Phase Diagram. *J. Chem. Phys.* **2019**, *150*, 060901.

(9) Zheligovskaya, E. A.; Malenkov, G. G. Crystalline Water Ices. *Russ. Chem. Rev.* **2006**, *75*, 57–76.

(10) Salzmann, C. G.; Radaelli, P. G.; Slater, B.; Finney, J. L. The Polymorphism of Ice: Five Unresolved Questions. *Phys. Chem. Chem. Phys.* **2011**, *13*, 18468–18480.

(11) Loerting, T.; Fuentes-Landete, V.; Tonauer, C. M.; Gasser, T. M. Open Questions on the Structures of Crystalline Water Ices. *Commun. Chem.* **2020**, *3*, 109.

(12) Salzmann, C. G.; Radaelli, P. G.; Hallbrucker, A.; Mayer, E.; Finney, J. L. The Preparation and Structures of Hydrogen Ordered Phases of Ice. *Science* **2006**, *311*, 1758.

(13) Malenkov, G. Liquid Water and Ices: Understanding the Structure and Physical Properties. *J. Phys.: Condens. Matter* **2009**, *21*, 283101.

(14) Walrafen, G. E. Raman Spectral Studies of Water Structure. *J. Chem. Phys.* **1964**, *40*, 3249–3256.

(15) Bernal, J. D.; Fowler, R. H. A Theory of Water and Ionic Solutions, with Particular Reference to Hydrogen and Hydroxyl Ions. *J. Chem. Phys.* **1933**, *1*, 515–548.

(16) Gu, Y.; Zhu, X.-L.; Jiang, L.; Cao, J.-W.; Qin, X.-L.; Yao, S.-K.; Zhang, P. Comparative Analysis of Hydrogen Bond Vibrations in Ice VIII and VII. *J. Phys. Chem. C* **2019**, *123*, 14880–14883.

(17) Jiang, L.; Yao, S.-K.; Zhang, K.; Wang, Z.-R.; Luo, H.-W.; Zhu, X.-L.; Gu, Y.; Zhang, P. Exotic Spectra and Lattice Vibrations of Ice X Using the DFT Method. *Molecules* **2018**, *23*, 2780.

(18) Wang, Z.-R.; Zhu, X.-L.; Jiang, L.; Zhang, K.; Luo, H.-W.; Gu, Y.; Zhang, P. Investigations of the Hydrogen Bonds and Vibrational Spectra of Clathrate Ice XVI. *Materials* **2019**, *12*, 246.

(19) Zhang, K.; Zhang, P.; Wang, Z.-R.; Zhu, X.-L.; Lu, Y.-B.; Guan, C.-B.; Li, Y. DFT Simulations of the Vibrational Spectrum and Hydrogen Bonds of Ice XIV. *Molecules* **2018**, *23*, 1781.

(20) Moberg, D. R.; Sharp, P. J.; Paesani, F. Molecular-Level Interpretation of Vibrational Spectra of Ordered Ice Phases. *J. Phys. Chem. B* **2018**, *122*, 10572–10581.

(21) Fuentes-Landete, V.; Köster, K. W.; Böhmer, R.; Loerting, T. Thermodynamic and Kinetic Isotope Effects on the Order–disorder Transition of ice XIV to ice XII. *Phys. Chem. Chem. Phys.* **2018**, *20*, 21607–21616.

(22) Fan, X.; Bing, D.; Zhang, J.; Shen, Z.; Kuo, J.-L. Predicting the Hydrogen Bond Ordered Structures of Ice Ih, II, III, VI and Ice VII: DFT Methods with Localized Based Set. *Comput. Mater. Sci.* **2010**, *49*, S170–S175.

(23) Nakamura, T.; Matsumoto, M.; Yagasaki, T.; Tanaka, H. Thermodynamic Stability of Ice II and Its Hydrogen-Disordered Counterpart: Role of Zero-Point Energy. *J. Phys. Chem. B* **2016**, *120*, 1843–1848.

(24) Ruckenstein, E.; Shulgin, I. L.; Shulgin, L. I. Cooperativity in Ordinary Ice and Breaking of Hydrogen Bonds. *J. Phys. Chem. B* **2007**, *111*, 7114–7121.

(25) Zhang, X.; Sun, P.; Yan, T.; Huang, Y.; Ma, Z.; Zou, B.; Zheng, W.; Zhou, J.; Gong, Y.; Sun, C. Q. Water's Phase Diagram: From the Notion of Thermodynamics to Hydrogen-bond Cooperativity. *Prog. Solid State Chem.* **2015**, *43*, 71–81.

(26) Xantheas, S. S. Cooperativity and Hydrogen Bonding Network in Water Clusters. *Chem. Phys.* **2000**, *258*, 225–231.

(27) Silvi, B.; Ratajczak, H. Hydrogen Bonding and Delocalization in the ELF Analysis Approach. *Phys. Chem. Chem. Phys.* **2016**, *18*, 27442–27449.

(28) Murray, É. D.; Galli, G. Dispersion Interactions and Vibrational Effects in Ice as a Function of Pressure: A First Principles Study. *Phys. Rev. Lett.* **2012**, *108*, 105502.

(29) Herrero, C. P.; Ramírez, R. Topological Characterization of Crystalline Ice Structures from Coordination Sequences. *Phys. Chem. Chem. Phys.* **2013**, *15*, 16676–16685.

(30) Konkoli, Z.; Cremer, D. A New Way of Analyzing Vibrational Spectra. I. Derivation of Adiabatic Internal Modes. *Int. J. Quantum Chem.* **1998**, *67*, 1–9.

(31) Konkoli, Z.; Larsson, J. A.; Cremer, D. A New Way of Analyzing Vibrational Spectra. II. Comparison of Internal Mode Frequencies. *Int. J. Quantum Chem.* **1998**, *67*, 11–27.

(32) Konkoli, Z.; Cremer, D. A New Way of Analyzing Vibrational Spectra. III. Characterization of Normal Vibrational Modes in terms of Internal Vibrational Modes. *Int. J. Quantum Chem.* **1998**, *67*, 29–40.

(33) Konkoli, Z.; Larsson, J. A.; Cremer, D. A New Way of Analyzing Vibrational Spectra. IV. Application and Testing of Adiabatic Modes within the Concept of the Characterization of Normal Modes. *Int. J. Quantum Chem.* **1998**, *67*, 41–55.

(34) Cremer, D.; Larsson, J. A.; Kraka, E. *Theoretical and Computational Chemistry*; Parkanyi, C., Ed.; Elsevier: Amsterdam, 1998; pp 259–327.

(35) Wilson, E. B.; Decius, J. C.; Cross, P. C. *Molecular Vibrations: The Theory of Infrared and Raman Vibrational Spectra*; McGraw-Hill: New York, NY, USA, 1955.

(36) Herzberg, G. *Molecular Spectra and Molecular Structure. Volume II: Infrared and Raman Spectra of Polyatomic Molecules*; Krieger Publishing Co.: New York, NY, USA, 1991.

(37) Zou, W.; Tao, Y.; Freindorf, M.; Cremer, D.; Kraka, E. Local Vibrational Force Constants - from the Assessment of Empirical Force Constants to the Description of Bonding in Large Systems. *Chem. Phys. Lett.* **2020**, *748*, 137337.

(38) Kraka, E.; Zou, W.; Tao, Y. Decoding Chemical Information from Vibrational Spectroscopy Data: Local Vibrational Mode Theory. *Wiley Interdiscip. Rev.: Comput. Mol. Sci.* **2020**, *10*, 1480.

(39) Delgado, A. A. A.; Sethio, D.; Munar, I.; Aviyente, V.; Kraka, E. Local Vibrational Mode Analysis of Ion–Solvent and Solvent–Solvent Interactions for Hydrated Ca<sup>2+</sup> Clusters. *J. Chem. Phys.* **2020**, *153*, 224303.

(40) Srinivas, R.; Verma, N.; Kraka, E.; Larson, E. C. Deep Learning-Based Ligand Design Using Shared Latent Implicit Fingerprints from Collaborative Filtering. *J. Chem. Inf. Model.* **2021**, *61*, 2159–2174.

(41) Freindorf, M.; Kraka, E. Critical Assessment of the FeC and CO Bond strength in Carboxymyoglobin - A QM/MM Local Vibrational Mode Study. *J. Mol. Model.* **2020**, *26*, 281.

(42) Verma, N.; Tao, Y.; Kraka, E. Systematic Detection and Characterization of Hydrogen Bonding in Proteins via Local Vibrational Modes. *J. Phys. Chem. B* **2021**, *125*, 2551–2565.

(43) Zou, W.; Cremer, D. C<sub>2</sub> in a Box: Determining its Intrinsic Bond Strength for the Ground State. *Chem.—Eur. J.* **2016**, *22*, 4087–4099.

(44) Kalescky, R.; Kraka, E.; Cremer, D. Identification of the Strongest Bonds in Chemistry. *J. Phys. Chem. A* **2013**, *117*, 8981–8995.

(45) Setiawan, D.; Sethio, D.; Cremer, D.; Kraka, E. From Strong to Weak NF Bonds: On the Design of a New Class of Fluorinating Agents. *Phys. Chem. Chem. Phys.* **2018**, *20*, 23913–23927.

(46) Humason, A.; Zou, W.; Cremer, D. 11,11-Dimethyl-1,6-methano[10]annulene-An Annulene with an Ultralong CC Bond or a Fluxional Molecule? *J. Phys. Chem. A* **2014**, *119*, 1666–1682.



- (47) Kalescky, R.; Kraka, E.; Cremer, D. Are Carbon-Halogen Double and Triple Bonds Possible? *Int. J. Quantum Chem.* **2014**, *114*, 1060–1072.
- (48) Kalescky, R.; Zou, W.; Kraka, E.; Cremer, D. Quantitative Assessment of the Multiplicity of Carbon-Halogen Bonds: Carbenium and Halonium Ions with F, Cl, Br, and I. *J. Phys. Chem. A* **2014**, *118*, 1948–1963.
- (49) Kraka, E.; Larsson, J. A.; Cremer, D. *Computational Spectroscopy*; Grunenberg, J., Ed.; Wiley: New York, 2010; pp 105–149.
- (50) Larsson, J. A.; Cremer, D. Theoretical Verification and Extension of the McKean Relationship between Bond Lengths and Stretching Frequencies. *J. Mol. Struct.* **1999**, *485–486*, 385–407.
- (51) Cremer, D.; Kraka, E. From Molecular Vibrations to Bonding, Chemical Reactions, and Reaction Mechanism. *Curr. Org. Chem.* **2010**, *14*, 1524–1560.
- (52) Cremer, D.; Wu, A.; Larsson, A.; Kraka, E. Some Thoughts about Bond Energies, Bond Lengths, and Force Constants. *J. Mol. Model.* **2000**, *6*, 396–412.
- (53) Kraka, E.; Cremer, D. Weaker Bonds with Shorter Bond Lengths. *Rev. Proc. Quim.* **2012**, *6*, 31–34.
- (54) Setiawan, D.; Kraka, E.; Cremer, D. Hidden Bond Anomalies: The Peculiar Case of the Fluorinated Amine Chalcogenides. *J. Phys. Chem. A* **2015**, *119*, 9541–9556.
- (55) Kraka, E.; Setiawan, D.; Cremer, D. Re-Evaluation of the Bond Length-Bond Strength Rule: The Stronger Bond Is not Always the Shorter Bond. *J. Comput. Chem.* **2015**, *37*, 130–142.
- (56) Delgado, A. A. A.; Humason, A.; Kalescky, R.; Freindorf, M.; Kraka, E. Exceptionally Long Covalent CC Bonds - A Local Vibrational Mode Study. *Molecules* **2021**, *26*, 950.
- (57) Zhao, L.; Zhi, M.; Frenking, G. The Strength of a Chemical Bond. *Int. J. Quantum Chem.* **2021**, No. e26773.
- (58) Oliveira, V.; Kraka, E.; Cremer, D. The Intrinsic Strength of the Halogen Bond: Electrostatic and Covalent Contributions Described by Coupled Cluster Theory. *Phys. Chem. Chem. Phys.* **2016**, *18*, 33031–33046.
- (59) Oliveira, V.; Kraka, E.; Cremer, D. Quantitative Assessment of Halogen Bonding Utilizing Vibrational Spectroscopy. *Inorg. Chem.* **2016**, *56*, 488–502.
- (60) Oliveira, V.; Cremer, D. Transition from Metal-Ligand Bonding to Halogen Bonding Involving a Metal as Halogen Acceptor: A Study of Cu, Ag, Au, Pt, and Hg Complexes. *Chem. Phys. Lett.* **2017**, *681*, 56–63.
- (61) Yannacone, S.; Oliveira, V.; Verma, N.; Kraka, E. A Continuum from Halogen Bonds to Covalent Bonds: Where Do  $\lambda^3$  Iodanes Fit? *Inorganics* **2019**, *7*, 47.
- (62) Oliveira, V. P.; Kraka, E.; Machado, F. B. C. Pushing 3c-4e Bonds to the Limit: A Coupled Cluster Study of Stepwise Fluorination of First-Row Atoms. *Inorg. Chem.* **2019**, *58*, 14777–14789.
- (63) Oliveira, V. P.; Marcial, B. L.; Machado, F. B. C.; Kraka, E. Metal-Halogen Bonding Seen through the Eyes of Vibrational Spectroscopy. *Materials* **2020**, *13*, 55.
- (64) Setiawan, D.; Kraka, E.; Cremer, D. Description of Pnictogen Bonding with the help of Vibrational Spectroscopy-The Missing Link Between Theory and Experiment. *Chem. Phys. Lett.* **2014**, *614*, 136–142.
- (65) Setiawan, D.; Kraka, E.; Cremer, D. Strength of the Pnictogen Bond in Complexes Involving Group VA Elements N, P, and As. *J. Phys. Chem. A* **2014**, *119*, 1642–1656.
- (66) Setiawan, D.; Cremer, D. Super-Pnictogen Bonding in the Radical Anion of the Fluorophosphine Dimer. *Chem. Phys. Lett.* **2016**, *662*, 182–187.
- (67) Oliveira, V.; Cremer, D.; Kraka, E. The Many Facets of Chalcogen Bonding: Described by Vibrational Spectroscopy. *J. Phys. Chem. A* **2017**, *121*, 6845–6862.
- (68) Oliveira, V.; Kraka, E. Systematic Coupled Cluster Study of Noncovalent Interactions Involving Halogens, Chalcogens, and Pnictogens. *J. Phys. Chem. A* **2017**, *121*, 9544–9556.
- (69) Sethio, D.; Oliveira, V.; Kraka, E. Quantitative Assessment of Tetrel Bonding Utilizing Vibrational Spectroscopy. *Molecules* **2018**, *23*, 2763.
- (70) Zhang, X.; Dai, H.; Yan, H.; Zou, W.; Cremer, D. B-H... $\pi$  Interaction: A New Type of Nonclassical Hydrogen Bonding. *J. Am. Chem. Soc.* **2016**, *138*, 4334–4337.
- (71) Zou, W.; Zhang, X.; Dai, H.; Yan, H.; Cremer, D.; Kraka, E. Description of an Unusual Hydrogen Bond Between Carborane and a Phenyl Group. *J. Organomet. Chem.* **2018**, *865*, 114–127.
- (72) Tao, Y.; Qiu, Y.; Zou, W.; Nanayakkara, S.; Yannacone, S.; Kraka, E. In Situ Assessment of Intrinsic Strength of X-I...OA Type Halogen Bonds in Molecular Crystals with Periodic Local Vibrational Mode Theory. *Molecules* **2020**, *25*, 1589.
- (73) Kalescky, R.; Zou, W.; Kraka, E.; Cremer, D. Local Vibrational Modes of the Water Dimer - Comparison of Theory and Experiment. *Chem. Phys. Lett.* **2012**, *554*, 243–247.
- (74) Kalescky, R.; Kraka, E.; Cremer, D. Local Vibrational Modes of the Formic Acid Dimer - The Strength of the Double H-Bond. *Mol. Phys.* **2013**, *111*, 1497–1510.
- (75) Freindorf, M.; Kraka, E.; Cremer, D. A Comprehensive Analysis of Hydrogen Bond Interactions Based on Local Vibrational Modes. *Int. J. Quantum Chem.* **2012**, *112*, 3174–3187.
- (76) Kalescky, R.; Zou, W.; Kraka, E.; Cremer, D. Vibrational Properties of the Isotopomers of the Water Dimer Derived from Experiment and Computations. *Aust. J. Chem.* **2014**, *67*, 426.
- (77) Tao, Y.; Zou, W.; Jia, J.; Li, W.; Cremer, D. Different Ways of Hydrogen Bonding in Water - Why Does Warm Water Freeze Faster than Cold Water? *J. Chem. Theory Comput.* **2017**, *13*, 55–76.
- (78) Tao, Y.; Zou, W.; Kraka, E. Strengthening of Hydrogen Bonding With the Push-Pull Effect. *Chem. Phys. Lett.* **2017**, *685*, 251–258.
- (79) Freindorf, M.; Tao, Y.; Sethio, D.; Cremer, D.; Kraka, E. New Mechanistic Insights into the Claisen Rearrangement of Chorismate - A Unified Reaction Valley Approach Study. *Mol. Phys.* **2018**, *117*, 1172–1192.
- (80) Makoš, M. Z.; Freindorf, M.; Sethio, D.; Kraka, E. New Insights into Fe-H<sub>2</sub> and Fe-H<sup>-</sup> Bonding of a [NiFe] Hydrogenase Mimic - A Local Vibrational Mode Study. *Theor. Chem. Acc.* **2019**, *138*, 76.
- (81) Lyu, S.; Beiranvand, N.; Freindorf, M.; Kraka, E. Interplay of Ring Puckering and Hydrogen Bonding in Deoxyribonucleosides. *J. Phys. Chem. A* **2019**, *123*, 7087–7103.
- (82) Yannacone, S. F.; Sethio, D.; Kraka, E. Quantitative Assessment of Intramolecular Hydrogen Bonds in Neutral Histidine. *Theor. Chem. Acc.* **2020**, *139*, 125.
- (83) Beiranvand, N.; Freindorf, M.; Kraka, E. Hydrogen Bonding in Natural and Unnatural Base Pairs - Explored with Vibrational Spectroscopy. *Molecules* **2021**, *26*, 2268.
- (84) Tao, Y.; Zou, W.; Sethio, D.; Verma, N.; Qiu, Y.; Tian, C.; Cremer, D.; Kraka, E. In Situ Measure of Intrinsic Bond Strength in Crystalline Structures: Local Vibrational Mode Theory for Periodic Systems. *J. Chem. Theory Comput.* **2019**, *15*, 1761–1776.
- (85) Dunnington, B. D.; Schmidt, J. R. Generalization of Natural Bond Orbital Analysis to Periodic Systems: Applications to Solids and Surfaces via Plane-Wave Density Functional Theory. *J. Chem. Theory Comput.* **2012**, *8*, 1902–1911.
- (86) Röttger, K.; Endriss, A.; Ihringer, J.; Doyle, S.; Kuhs, W. F. Lattice constants and thermal expansion of H<sub>2</sub>O and D<sub>2</sub>O Ice Ih between 10 and 265 K. Addendum. *Acta Crystallogr., Sect. B: Struct. Sci.* **2012**, *68*, 91.
- (87) Line, C. M. B.; Whitworth, R. W. A High Resolution Neutron Powder Diffraction Study of D<sub>2</sub>O ice XI. *J. Chem. Phys.* **1996**, *104*, 10008.
- (88) Londono, J. D.; Kuhs, W. F.; Finney, J. L. Neutron Diffraction Studies of ices III and IX on under-pressure and Recovered Samples. *J. Chem. Phys.* **1993**, *98*, 4878.
- (89) Kuhs, W. F.; Finney, J. L.; Vettier, C.; Bliss, D. V. Structure and Hydrogen Ordering in Ices VI, VII, and VIII by Neutron Powder Diffraction. *J. Chem. Phys. B* **1984**, *81*, 3612.
- (90) Kamb, B.; Prakash, A.; Knobler, C. Structure of ice V. *Acta Crystallogr.* **1967**, *22*, 706.
- (91) Lobban, C.; Finney, J. L.; Kuhs, W. F. The Structure of a New Phase of Ice. *Nature* **1998**, *391*, 268–270.



- (92) Salzmann, C. G.; Radaelli, P. G.; Mayer, E.; Finney, J. L. Ice XV: A New Thermodynamically Stable Phase of Ice. *Phys. Rev. Lett.* **2009**, *103*, 105701.
- (93) Salzmann, C. G.; Loveday, J. S.; Rosu-Finsen, A.; Bull, C. L. Structure and Nature of Ice XIX. *Nat. Commun.* **2021**, *12*, 3162.
- (94) Yamane, R.; Komatsu, K.; Gouchi, J.; Uwatoko, Y.; Machida, S.; Hattori, T.; Ito, H.; Kagi, H. Experimental Evidence for the Existence of a Second Partially-ordered Phase of Ice VI. *Nat. Commun.* **2021**, *12*, 1129.
- (95) Gasser, T. M.; Thoeny, A. V.; Fortes, A. D.; Loerting, T. Structural Characterization of Ice XIX as the Second Polymorph Related to Ice VI. *Nat. Commun.* **2021**, *12*, 1128.
- (96) Kamb, B. Ice. II. A Proton-ordered Form of Ice. *Acta Crystallogr.* **1964**, *17*, 1437–1449.
- (97) Lobban, C.; Finney, J. L.; Kuhs, W. F. The p–T Dependency of the Ice II Crystal Structure and the Effect of Helium Inclusion. *J. Chem. Phys.* **2002**, *117*, 3928.
- (98) Engelhardt, H.; Kamb, B. Structure of Ice IV, a Metastable High-pressure Phase. *J. Chem. Phys.* **1981**, *75*, 5887.
- (99) del Rosso, L.; Celli, M.; Ulivi, L. New Porous Water Ice Metastable at Atmospheric Pressure Obtained by Emptying a Hydrogen-filled Ice. *Nat. Commun.* **2016**, *7*, 13394.
- (100) Hayward, J. A.; Reimers, J. R. Unit Cells for the Simulation of Hexagonal Ice. *J. Chem. Phys.* **1997**, *106*, 1518.
- (101) Herrero, C. P.; Ramírez, R. Configurational Entropy of Hydrogen-disordered Ice Polymorphs. *J. Chem. Phys.* **2014**, *140*, 234502.
- (102) Kuo, J.-L. The Low-temperature Proton-ordered Phases of Ice Predicted by ab initio Methods. *Phys. Chem. Chem. Phys.* **2005**, *7*, 3733–3737.
- (103) Matsumoto, M.; Yagasaki, T.; Tanaka, H. Novel Algorithm to Generate Hydrogen-Disordered Ice Structures. *J. Chem. Inf. Model.* **2021**, *61*, 2542–2546.
- (104) Kuo, J.-L.; Singer, S. J. Graph Invariants for Periodic Systems: Towards Predicting Physical Properties from the Hydrogen Bond Topology of Ice. *Phys. Rev. E: Stat., Nonlinear, Soft Matter Phys.* **2003**, *67*, 016114.
- (105) Brandenburg, J. G.; Maas, T.; Grimme, S. Benchmarking DFT and Semiempirical Methods on Structures and Lattice Energies for Ten Ice Polymorphs. *J. Chem. Phys.* **2015**, *142*, 124104.
- (106) Lee, K.; Murray, E. D.; Kong, L. Z.; Lundqvist, B. I.; Langreth, D. C. Higher-accuracy van der Waals Density Functional. *Phys. Rev. B: Condens. Matter Mater. Phys.* **2010**, *82*, 081101.
- (107) Santra, B.; Klimeš, J.; Tkatchenko, A.; Alfè, D.; Slater, B.; Michaelides, A.; Car, R.; Scheffler, M. On the Accuracy of van der Waals Inclusive Density-functional Theory Exchange-correlation Functionals for Ice at Ambient and High Pressures. *J. Chem. Phys.* **2013**, *139*, 154702.
- (108) Gillan, M. J.; Alfè, D.; Michaelides, A. Perspective: How Good is DFT for Water? *J. Chem. Phys.* **2016**, *144*, 130901.
- (109) Sun, J.; Remsing, R. C.; Zhang, Y.; Sun, Z.; Ruzsinszky, A.; Peng, H.; Yang, Z.; Paul, A.; Waghmare, U.; Wu, X.; Klein, M. L.; Perdew, J. P. Accurate First-principles Structures and Energies of Diversely Bonded Systems from an Efficient Density Functional. *Nat. Chem.* **2016**, *8*, 831–836.
- (110) Chen, J.; Zen, A.; Brandenburg, J. G.; Alfè, D.; Michaelides, A. Evidence for Stable Square Ice from Quantum Monte Carlo. *Phys. Rev. B* **2016**, *94*, 220102.
- (111) Brandenburg, J. G.; Zen, A.; Alfè, D.; Michaelides, A. Interaction between Water and Carbon Nanostructures: How Good are Current Density Functional Approximations? *J. Chem. Phys.* **2019**, *151*, 164702.
- (112) Dovesi, R.; Erba, A.; Orlando, R.; Zicovich-Wilson, C. M.; Civalieri, B.; Maschio, L.; Rérat, M.; Casassa, S.; Baima, J.; Salustro, S.; Kirtman, B. Quantum-Mechanical Condensed Matter Simulations With CRYSTAL. *Wiley Interdiscip. Rev.: Comput. Mol. Sci.* **2018**, *8*, No. e1360.
- (113) Dovesi, R.; Saunders, V. R.; Roetti, C.; Orlando, R.; Zicovich-Wilson, C. M.; Pascale, F.; Civalieri, B.; Doll, K.; Harrison, N. M.; Bush, I. J.; D'Arco, P.; Llunell, M.; Causà, M.; Noël, L.; Maschio, Y.; Erba, A.; Rérat, M.; Casassa, S. *CRYSTAL17 User's Manual*; University of Torino: Torino, 2017.
- (114) Becke, A. D. Density-functional Exchange-energy Approximation with Correct Asymptotic Behavior. *Phys. Rev. A: At., Mol., Opt. Phys.* **1988**, *38*, 3098.
- (115) Lee, C.; Yang, W.; Parr, R. G. Development of the Colle-Salvetti Correlation-energy Formula into a Functional of the Electron Density. *Phys. Rev. B: Condens. Matter Mater. Phys.* **1988**, *37*, 785.
- (116) Grimme, S.; Antony, J.; Ehrlich, S.; Krieg, H. A Consistent and Accurate ab initio Parametrization of Density Functional Dispersion Correction (DFT-D) for the 94 Elements H–Pu. *J. Chem. Phys.* **2010**, *132*, 154104.
- (117) Grimme, S.; Ehrlich, S.; Goerigk, L. Effect of the Damping Function in Dispersion Corrected Density Functional Theory. *J. Comput. Chem.* **2011**, *32*, 1456–1465.
- (118) Dill, J. D.; Pople, J. A. Self-Consistent Molecular Orbital Methods. XV. Extended Gaussian-Type Basis Sets for Lithium, Beryllium, and Boron. *J. Chem. Phys.* **1975**, *62*, 2921–2923.
- (119) Hariharan, P. C.; Pople, J. A. The influence of polarization functions on molecular orbital hydrogenation energies. *Theor. Chem. Acc.* **1973**, *28*, 213–222.
- (120) Csonka, G. I.; Ruzsinszky, A.; Perdew, J. P. Proper Gaussian Basis Sets for Density Functional Studies of Water Dimers and Trimers. *J. Phys. Chem. B* **2005**, *109*, 21471–21475.
- (121) Kresse, G.; Furthmüller, J. Efficient Iterative Schemes for Ab Initio Total-Energy Calculations using a Plane-Wave Basis Set. *Phys. Rev. B: Condens. Matter Mater. Phys.* **1996**, *54*, 11169–11186.
- (122) Hafner, J. Ab-Initio Simulations of Materials using VASP: Density-Functional Theory and Beyond. *J. Comput. Chem.* **2008**, *29*, 2044–2078.
- (123) Blöchl, P. E. Projector Augmented-Wave Method. *Phys. Rev. B: Condens. Matter Mater. Phys.* **1994**, *50*, 17953.
- (124) Kresse, G.; Joubert, D. From Ultrasoft Pseudopotentials to the Projector Augmented-Wave Method. *Phys. Rev. B: Condens. Matter Mater. Phys.* **1999**, *59*, 1758.
- (125) Monkhorst, H.; Pack, J. Special Points for Brillouin-Zone Integrations. *Phys. Rev. B: Solid State* **1976**, *13*, 5188–5192.
- (126) Boole, G. A. *A Treatise on the Calculus of Finite Differences*; Cosimo Classics, 2007.
- (127) Pascale, F.; Zicovich-Wilson, C. M.; López Gejo, F.; Civalieri, B.; Orlando, R.; Dovesi, R. The Calculation of the Vibrational Frequencies of Crystalline Compounds and Its Implementation in the CRYSTAL Code. *J. Comput. Chem.* **2004**, *25*, 888–897.
- (128) Tukey, J. W. *Exploratory Data Analysis*; Pearson, 1977.
- (129) Zou, W.; Tao, Y.; Freindorf, M.; Makoš, M. Z.; Verma, N.; Cremer, D.; Kraka, E. Local Vibrational Mode Analysis (LModeA). *Computational and Theoretical Chemistry Group (CATCO)*; Southern Methodist University: Dallas, TX, USA, 2021.
- (130) Momma, K.; Izumi, F. VESTA 3 for Three-dimensional Visualization of Crystal, Volumetric and Morphology Data. *J. Appl. Crystallogr.* **2011**, *44*, 1272–1276.
- (131) Caldeweyher, E.; Mewes, J.-M.; Ehlert, S.; Grimme, S. Extension and Evaluation of the D4 London-dispersion Model for Periodic Systems. *Phys. Chem. Chem. Phys.* **2020**, *22*, 8499.
- (132) Hamann, D. R. H<sub>2</sub>O Hydrogen Bonding in Density-functional Theory. *Phys. Rev. B: Condens. Matter Mater. Phys.* **1997**, *55*, R10157.
- (133) Whalley, E. Energies of the Phases of Ice at Zero Temperature and Pressure. *J. Chem. Phys.* **1984**, *81*, 4087.
- (134) Leadbetter, A. J.; Ward, R. C.; Clark, J. W.; Tucker, P. A.; Matsuo, T.; Suga, H. The Equilibrium Low-temperature Structure of Ice. *J. Chem. Phys.* **1985**, *82*, 424.
- (135) Kamb, B.; Hamilton, W. C.; LaPlaca, S. J.; Prakash, A. Ordered Proton Configuration in Ice II, from Single-Crystal Neutron Diffraction. *J. Chem. Phys.* **1971**, *55*, 1934.
- (136) del Rosso, L.; Grazi, F.; Celli, M.; Colognesi, D.; Garcia-Sakai, V.; Ulivi, L. Refined Structure of Metastable Ice XVII from Neutron Diffraction Measurements. *J. Phys. Chem. C* **2016**, *120*, 26955–26959.

(137) Badger, R. M. A Relation Between Internuclear Distances and Bond Force Constants. *J. Chem. Phys.* **1934**, *2*, 128–131.

(138) Badger, R. M. The Relation Between Internuclear Distances and the Force Constants of Diatomic Molecules. *Phys. Rev.* **1935**, *48*, 284–285.

(139) Boyer, M. A.; Marsalek, O.; Heindel, J. P.; Markland, T. E.; McCoy, A. B.; Xantheas, S. S. Beyond Badger's Rule: The Origins and Generality of the Structure–Spectra Relationship of Aqueous Hydrogen Bonds. *J. Phys. Chem. Lett.* **2019**, *10*, 918–924.

(140) Libowitzky, E. Correlation of O–H Stretching Frequencies and O–H...O Hydrogen Bond Lengths in Minerals. *Monatsh. Chem.* **1999**, *130*, 1047–1059.

(141) Majerz, I. Directionality of Inter- and Intramolecular OHO Hydrogen Bonds: DFT Study Followed by AIM and NBO Analysis. *J. Phys. Chem. A* **2012**, *116*, 7992–8000.

(142) Bar-nun, A.; Herman, G.; Laufer, D.; Rappaport, M. L. Trapping and Release of Gases by Water Ice and Implications for Icy Bodies. *Icarus* **1985**, *63*, 317–332.

(143) Bertie, J. E.; Whalley, E. Infrared spectra of ices II, III, and V in the range 4000 to 350  $\text{cm}^{-1}$ . *J. Chem. Phys.* **1964**, *40*, 1646–1659.

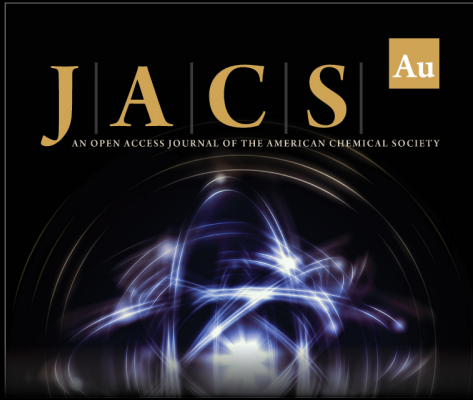
(144) Lu, Q.; Ali, I.; Li, J. Prediction of Properties from First Principles with Quantitative Accuracy: Six Representative Ice Phases. *New J. Chem.* **2020**, *44*, 21012–21020.

(145) Dunaeva, A. N.; Antsyshkin, D. V.; Kuskov, O. L. Phase Diagram of  $\text{H}_2\text{O}$ : Thermodynamic Functions of the Phase Transitions of High-Pressure Ices. *Sol. Syst. Res.* **2010**, *44*, 202–222.


(146) Knudson, M. D.; Desjarlais, M. P.; Lemke, R. W.; Mattsson, T. R.; French, M.; Nettelmann, N.; Redmer, R. Probing the Interiors of the Ice Giants: Shock Compression of Water to 700 GPa and 3.8  $\text{g}/\text{cm}^3$ . *Phys. Rev. Lett.* **2012**, *108*, 091102.


(147) Santra, B.; Klimeš, J.; Alfè, D.; Tkatchenko, A.; Slater, B.; Michaelides, A.; Car, R.; Scheffler, M. Hydrogen Bonds and van der Waals Forces in Ice at Ambient and High Pressures. *Phys. Rev. Lett.* **2011**, *107*, 185701.


(148) Nissan, A. H. The Hydrogen Bond Strength of Ice. *Nature* **1956**, *178*, 1411–1412.



**JACS** Au  
AN OPEN ACCESS JOURNAL OF THE AMERICAN CHEMICAL SOCIETY

 Editor-in-Chief  
**Prof. Christopher W. Jones**  
Georgia Institute of Technology, USA

**Open for Submissions** 

pubs.acs.org/jacsau  ACS Publications  
Most Trusted. Most Cited. Most Read.